To appear in Part 1, ApJ August 10, 2002 issue.

Collapse of Rotating Magnetized Molecular Cloud Cores and Mass Outflows

Kohji Tomisaka

Theoretical Astrophysics, National Astronomical Observatory, Mitaka, Tokyo 181-8588, Japan

tomisaka@th.nao.ac.jp

ABSTRACT

Collapse of rotating magnetized molecular cloud cores is studied with axisymmetric magnetohydrodynamical (MHD) simulations. Due to the change of the equation of state of the interstellar gas, molecular cloud cores experience several phases during the collapse. In the earliest isothermal run-away collapse ($n \lesssim 10^{10}\mathrm{H_2\,cm^{-3}}$), a pseudo-disk is formed and it continues to contract till an opaque core is formed at the center. In this disk, a number of MHD fast and slow shock pairs appear whose wave fronts are parallel to the disk. We assume the interstellar gas obeys a polytropic equation of state with the exponent of $\Gamma > 1$ above the critical density at which the core becomes optically thick against the thermal radiation from dusts $n_{\rm cr} \sim 10^{10}\mathrm{cm^{-3}}$. After the equation of state becomes hard, an adiabatic quasistatic core forms at the center (the first core), which is separated from the isothermal contracting pseudo-disk by the accretion shock front facing radially outwards. By the effect of the magnetic tension, the angular momentum is transferred from the disk mid-plane to the surface. The gas with an excess angular momentum near the surface is finally ejected, which explains the molecular bipolar outflow. Two types of outflows are found. When the poloidal magnetic field is strong (its energy is comparable to the thermal one), a U-shaped outflow is formed, in which gas is mainly outflowing through a region whose shape looks like a capital letter U at a finite distance from the rotation axis. The gas is accelerated by the centrifugal force and the magnetic pressure gradient of the toroidal component. The other is a turbulent outflow in which magnetic field lines and velocity fields seem to be randomly oriented. In this case, globally the gas moves out almost perpendicularly from the disk and the outflow looks like a capital letter I. In this case, although the gas is launched

by the centrifugal force, the magnetic force working along the poloidal field lines plays an important role to expand the outflow. The continuous mass accretion leads to a quasistatic contraction of the first core. A second collapse due to the dissociation of H_2 occurs in it. Finally another less-massive quasistatic core is formed by atomic hydrogen (the second core). At the same time, it is found that another outflow is ejected around the second atomic core, which seems to correspond to the optical jets or the fast neutral winds.

Subject headings: ISM: clouds — ISM: magnetic fields — stars: formation — ISM: jets and outflows

1. Introduction

Star formation has been a long-standing target in astrophysics. The infrared protostar distribution revealed that the molecular cloud cores, which coincide with relatively high-density part ($n \sim 10^4 \mathrm{cm}^{-3}$) of the molecular clouds, are the sites of star formation. The observed molecular cloud cores are divided into two categories: those observed associated with and without protostars. The molecular cloud cores without protostars are called starless cores or prestellar cores and are considered younger than those associated with protostars (protostellar cores). From a theoretical point of view, clouds or cloud cores experience the isothermal run-away collapse first and then accretion on to the stellar core develops (Larson 1969). In the former collapse, the central density increases greatly in a finite time scale ($\simeq$ free-fall time). A number of prestellar cores show the inflow motions (e.g. in L1544 rotation and infall velocities $\sim 0.1 \mathrm{km\,s}^{-1}$ are observed by Ohashi et al. (2000)). This indicates that they are in the dynamically contracting phase, or in other words, in the run-away collapse (Ciolek & Basu 2000). After the epoch when the dust thermal emissions are trapped in the central part of the cloud ($n_c \sim 10^{10} \mathrm{cm}^{-3}$), an adiabatic core is formed at the center and isothermal gas continues to accrete on to the core. The molecular cloud core in this phase is observed as a protostellar core. It is shown that the dynamical evolution of the cloud core is characterized by the sequence from prestellar cores to protostellar cores.

Dynamical collapse of the magnetized clouds is studied by many authors (Scott & Black 1980; Phillips 1986a,b; Dorfi 1982, 1989; Bentz 1984; Mouschovias & Morton 1991, 1992; Fiedler & Mouschovias 1992, 1993; Basu & Mouschovias 1994; Tomisaka 1995, 1996; Nakamura et al. 1999). Rotating cloud collapse has been attacked seriously with numerical simulations by many authors (Bodenheimer, Tohline, & Black 1980; Norman, Wilson, & Barton 1980; Wood 1982; Narita, Hayashi, & Miyama 1984; Truelove et al. 1997, 1998; Tsuribe & Inutsuka 1999a,b). However, a restricted number of articles are published regarding the

dynamical contraction of the cloud with both rotation and magnetic fields (Dorfi 1982, 1989; Basu & Mouschovias 1994, 1995; Boss 2000, 2001); for quasistatic evolution see Tomisaka, Ikeuchi, & Nakamura (1990). These researches are confined to the relatively early prestellar stage.

Is it sufficient to consider the effects of the rotational motion and the magnetic fields separately? In the dynamical contraction phase, the molecular outflow is believed to be driven by the cooperative effect of the magnetic fields and rotation motions (Tomisaka 1998). The toroidal magnetic fields are generated from the poloidal ones by the effect of rotation motions (the Ampere's law). The torque works only when the poloidal and toroidal magnetic fields coexist, since the Lorentz force in ϕ-direction works between the poloidal magnetic field and the poloidal current which makes the toroidal magnetic field. This magnetic torque leads the magnetic angular momentum transfer along the magnetic field line, which is important to eject the outflow. Since the outflow brings the excess angular momentum, the amount of angular momentum that remains in a protostar and thus in a new-born star is reduced by a factor from 10^{-2} to 10^{-3} from that of the parent molecular cloud core (Tomisaka 2000). Numerical simulations have confirmed that no outflows are observed in the magnetized and non-rotating cloud (Scott & Black 1980; Tomisaka 1996) or the rotating and non-magnetized cloud (Norman, Wilson, & Barton 1980). Therefore, rotation and magnetic fields are both essential to the evolution of molecular cloud cores. In the present paper, we study the dynamical contraction of the magnetized and rotating cloud.

Cooperative effects of magnetic fields and the rotation motions become important after the adiabatic core is formed at the center of the cloud core (Tomisaka 1998). Therefore, the evolution throughout from the prestellar to protostellar core should be studied.

Plan of this paper is as follows: in §2, model and numerical method are described. As the initial condition, we choose a slowly rotating cloud threaded by purely poloidal magnetic fields (no toroidal magnetic fields). And we follow the evolution using magnetohydrodynamical simulations. Section 3 is devoted to the numerical results. In this section we compare clouds with strong magnetic fields and those with weak magnetic fields. This shows us that completely different two types of outflows are formed in the respective clouds. Another comparison is made between fast and slow rotators. In §4, we discuss the evolution till the second core, which becomes actually a new-born star, is formed. It is found that another outflow is found around the second core, which seems to correspond to the optical jets or high speed neutral winds. We also discuss whether the mass inflow/outflow rates and the momentum outflow rates observed in molecular bipolar outflows are explained or not.

2. Model and Numerical Method

To study the dynamical contraction, we consider an isothermal cylindrical cloud in hydrostatic balance with infinite length as the initial state. In several star forming regions such as Taurus and Ophiucus regions, we often find filamentary molecular clouds. However, the relationship is controversial between the direction of magnetic fields and that of the filament: in ρ Ophiuchi clouds, L1709, L1729 (Loren 1989), and L1755 (Goodman et al. 1995) have filamentary shapes and the directions of the major axes agree with the direction of magnetic field lines which are measured by the near IR polarization observations of the background field stars. While in B216-217 clouds in Taurus, the magnetic field lines seem to run perpendicular to the major axes of the dark clouds, even if they seem filamentary(Heyer et al. 1987; Goodman et al. 1992). In this paper, we examine the evolution of these magnetized filamentary clouds. We focus on the model in which magnetic field lines are parallel to the major axis of the filament and the case with perpendicular magnetic fields will be studied in a separate paper.

In terms of the gravitational potential ψ and the isothermal sound speed c_s, the radial distributions of density ρ, rotation speed v_ϕ, and magnetic field density B_z are calculated using the equation of hydrostatic balance as

$$\frac{v_\phi^2}{r} - \frac{\partial \psi}{\partial r} - \frac{c_s^2}{\rho}\frac{\partial \rho}{\partial r} - \frac{1}{8\pi\rho}\frac{\partial B_z^2}{\partial r} = 0, \tag{1}$$

and the Poisson equation for the self-gravity as

$$\frac{1}{r}\frac{\partial}{\partial r}\left(r\frac{\partial \psi}{\partial r}\right) = 4\pi G\rho, \tag{2}$$

where G represents the gravitational constant. This equation has a solution as follows (Stodółkiewicz 1963):

$$\rho_0(r) = \rho_{c0}\left(1 + \frac{r^2}{8H_c^2}\right)^{-2}, \tag{3}$$

$$v_{\phi(r)\,0} \equiv r\Omega_0(r) = r\Omega_{c0}\left(\frac{\rho}{\rho_c}\right)^{1/4} = r\Omega_{c0}\left(1 + \frac{r^2}{8H_c^2}\right)^{-1/2}, \tag{4}$$

and

$$B_{z\,0}(r) = B_{c0}\left(\frac{\rho}{\rho_c}\right)^{1/2} = B_{c0}\left(1 + \frac{r^2}{8H_c^2}\right)^{-1}, \tag{5}$$

with using the scale-height at the center,

$$H_c^2 = \frac{c_s^2 + B_{c0}^2/8\pi\rho_{c0}}{4\pi G\rho_{c0} - 2\Omega_{c0}^2}, \tag{6}$$

where ρ_{c0}, Ω_{c0}, and B_{c0} represent respectively the density, the angular rotation speed, and the magnetic flux density at the center of the cylindrical cloud ($r = 0$). This is the same hydrostatic configuration studied by Matsumoto, Hanawa, & Nakamura (1997). However, we assume no initial toroidal magnetic field $B_\phi = 0$ in contrast to them. The density distribution is assumed to extend till the radius where the thermal pressure $c_s^2\rho_s$ becomes equal to the external pressure $p_{\rm ext}$, where ρ_s represents the density at the surface of the cylindrical cloud. The solution contains three non-dimensional parameters characterizing the distribution after adopting natural normalization such as for distance $r' \equiv r/H \equiv r/[c_s/(4\pi G\rho_s)^{1/2}]$, for time $t' \equiv t/\tau_{\rm ff} \equiv t/[1/(4\pi G\rho_s)^{1/2}]$, and for density $\rho' \equiv \rho/\rho_s \equiv c_s^2\rho(r)/p_{\rm ext}$. We summarized the conversion factors from non-dimensional to physical quantities in Table 1. The first parameter characterizing the initial state is related to the magnetic to thermal pressure ratio as

$$\alpha \equiv B_z(r)^2/4\pi\rho(r)c_s^2 = B_{c0}^2/4\pi\rho_{c0}c_s^2, \tag{7}$$

where $\alpha = 2/\beta$ if we use the plasma β. The second one is related to the angular rotation speed as

$$\Omega' = \Omega_{c0}/(4\pi G\rho_s)^{1/2}. \tag{8}$$

Finally the third one is the surface to center density ratio as

$$F \equiv \rho_{c0}/\rho_s. \tag{9}$$

The scale-height at the center H_c is rewritten using these non-dimensional parameters as

$$H_c'^2 = \frac{H_c^2}{c_s^2/4\pi G\rho_s} = \frac{1+\alpha/2}{F - 2\Omega'^2}. \tag{10}$$

From this equation, it is shown that a hydrostatic balance is achieved only when $F > 2\Omega'^2$, i.e., $4\pi G\rho_{c0} > 2\Omega_{c0}^2$ in dimensional form. Matsumoto, Hanawa, & Nakamura (1994)'s β parameter, which represents the ratio of the centrifugal force to the thermal pressure force, is expressed using our parameters as

$$\begin{aligned} \beta &= \frac{\rho(r)v_\phi(r)^2/r}{c_s^2 d\rho(r)/dr} \\ &= \frac{2\Omega_{c0}^2 H^2}{c_s^2} \\ &= 2\Omega'^2\frac{1+\alpha/2}{F-2\Omega'^2}. \end{aligned} \tag{11}$$

To initiate the cloud collapse, we added density perturbations with a small amplitude. The wavelength of the perturbation is taken equal to that of the most unstable Jeans mode

of this isothermal filament. Its linear stability is already studied by Matsumoto, Hanawa, & Nakamura (1994). They gave a fitting formula for the most unstable wavelength as follows:

$$\lambda_{\max}\left[\frac{c_s}{(4\pi G\rho_s)^{1/2}}\right]^{-1} \simeq \frac{2\pi\left(1+\alpha/2+\beta\right)^{1/2}}{0.72\left[\left(1+\alpha/2+\beta\right)^{1/3}-0.6\right]F^{1/2}}, \tag{12}$$

where we used equations (7), (9), and (11). Therefore, we take this most unstable wavelength and the initial density is assumed equal to

$$\rho(z,r) = \rho_0(r)\left[1+A\cos\left(\frac{2\pi z}{\lambda_{\max}}\right)\right], \tag{13}$$

for $-\lambda_{\max}/2 \le z \le \lambda_{\max}/2$. The amplitude of the perturbation A is taken equal to 0.1. Hereafter, we omit the primes which indicate the non-dimensional quantities, unless the quantities are confused with dimensional ones.

From calculations of one-dimensional, non-rotating, non-magnetized spherical cloud collapse, the effective equation of state of the gas forming a star is summarized as follows (Tohline 1982). The equation of state is determined by the balance between the radiative cooling and the compressional heating (Masunaga & Inutsuka 1999). Gas in the molecular cloud core with $\rho \sim 10^4 \mathrm{H_2\ cm^{-3}}$ obeys the isothermal equation of state with the temperature of $T_0 \sim 10\mathrm{K}$, in which the gas is mainly cooled by the thermal radiation from dusts. However, radiative hydrodynamical calculations (e.g.Masunaga & Inutsuka (1999)) have shown that the molecular gas becomes optically thick against such emissions, at the density approximately equal to $\rho_c = \rho_{\rm A} \sim 10^{10}\mathrm{H_2\ cm^{-3}}$. The gas becomes adiabatic beyond the density and a quasi-hydrostatic H_2 core forms which is supported by the thermal pressure (Larson 1969). This is called a first core. In this phase the polytropic exponent, Γ, of this molecular hydrogen gas is well approximated equal to 7/5, although Γ is as large as 5/3 while the temperature is quite low and neither rotational nor vibrational modes of the molecules are excited. Mass of the first core grows by continuous accretion and the central density and thus temperature increase with time. Finally, hydrogen molecules (H_2) dissociate into hydrogen atoms (H) when its temperature exceeds $T_{\rm dis} \simeq 10^3\mathrm{K}$. Typical density at which the temperature reaches $T_{\rm dis}$ is equal to $\rho_{\rm B} = \rho_{\rm A}(T_{\rm dis}/T_0)^{1/(\gamma-1)} \simeq 10^{15}\mathrm{H_2\ cm^{-3}}(T_{\rm dis}/10^3\mathrm{K})^{5/2}(T_0/10\mathrm{K})^{-5/2}$. The dissociation ends at the density $\rho_{\rm C} \simeq 10^{19}\mathrm{H_2\ cm^{-3}}$. Since the hydrogen dissociation reaction absorbs its thermal energy liberated by the compression, the polytropic exponent decreases as $\Gamma \simeq 1.1$. Finally forms an atomic hydrogen core, which is call the second core by Larson (1969). Since the constituent of the second core is atomic hydrogen, Γ becomes

$\simeq 5/3$. To include these changes, we adopt a multiple polytrope approximation as

$$p = \begin{cases} c_s^2 \rho, & \rho < \rho_{\rm A}, \\ c_s^2 \rho_A \left(\frac{\rho}{\rho_{\rm A}}\right)^{7/5}, & \rho_{\rm A} < \rho < \rho_{\rm B}, \\ c_s^2 \rho_A \left(\frac{\rho_{\rm B}}{\rho_{\rm A}}\right)^{7/5} \left(\frac{\rho}{\rho_{\rm B}}\right)^{1.1}, & \rho_{\rm B} < \rho < \rho_{\rm C}, \\ c_s^2 \rho_A \left(\frac{\rho_{\rm B}}{\rho_{\rm A}}\right)^{7/5} \left(\frac{\rho_{\rm C}}{\rho_{\rm B}}\right)^{1.1} \left(\frac{\rho}{\rho_{\rm C}}\right)^{5/3}, & \rho > \rho_{\rm C}, \end{cases} \tag{14}$$

with $\rho_{\rm A} = 10^{10} {\rm H}_2\,{\rm cm}^{-3}$, $\rho_{\rm B} = 10^{15} {\rm H}_2\,{\rm cm}^{-3}$, and $\rho_{\rm C} = 10^{19} {\rm H}_2\,{\rm cm}^{-3}$. This is similar to that adopted by Bate (1998). Since the equation of state is achieved by the balance of radiative loss and the compressional heating, the result obtained assuming the spherical symmetry might be incorrect if we apply it to the multidimensional simulations. However, as is seen later, the cores (the first and the second cores) are almost spherical and the approximation of the multiple polytropes is valid.

The basic equations to be solved are the magnetohydrodynamical equations and the Poisson equation for the gravitational potential. In cylindrical coordinates (z, r, ϕ) with $\partial/\partial\phi = 0$, the equations are expressed as follows:

$$\frac{\partial \rho}{\partial t} + \frac{\partial}{\partial z}(\rho v_z) + \frac{1}{r}\frac{\partial}{\partial r}(r \rho v_r) = 0, \tag{15}$$

$$\begin{aligned} \frac{\partial \rho v_z}{\partial t} &+ \frac{\partial}{\partial z}(\rho v_z v_z) + \frac{1}{r}\frac{\partial}{\partial r}(r \rho v_z v_r) = \\ &- c_s^2 \frac{\partial \rho}{\partial z} - \rho \frac{\partial \psi}{\partial z} + \frac{1}{4\pi}\left[-\frac{\partial B_\phi}{\partial z} B_\phi - \left(\frac{\partial B_r}{\partial z} - \frac{\partial B_z}{\partial r} \right) B_r \right], \end{aligned} \tag{16}$$

$$\begin{aligned} \frac{\partial \rho v_r}{\partial t} &+ \frac{\partial}{\partial z}(\rho v_r v_z) + \frac{1}{r}\frac{\partial}{\partial r}(r \rho v_r v_r) = \\ &- c_s^2 \frac{\partial \rho}{\partial r} - \rho \frac{\partial \psi}{\partial r} + \frac{1}{4\pi}\left[-\frac{1}{r}\frac{\partial}{\partial r}(r B_\phi) B_\phi + \left(\frac{\partial B_r}{\partial z} - \frac{\partial B_z}{\partial r} \right) B_z \right], \end{aligned} \tag{17}$$

$$\frac{\partial \rho r v_\phi}{\partial t} + \frac{\partial}{\partial z}(\rho r v_\phi v_z) + \frac{1}{r}\frac{\partial}{\partial r}(r \rho r v_\phi v_r) = \frac{r}{4\pi}\left[\frac{1}{r}\frac{\partial}{\partial r}(r B_\phi) B_r + \frac{\partial B_\phi}{\partial z} B_z \right] \tag{18}$$

$$\frac{\partial B_z}{\partial t} = \frac{1}{r}\frac{\partial}{\partial r}[r(v_z B_r - v_r B_z)], \tag{19}$$

$$\frac{\partial B_r}{\partial t} = -\frac{\partial}{\partial z}(v_z B_r - v_r B_z), \tag{20}$$

$$\frac{\partial B_\phi}{\partial t} = \frac{\partial}{\partial z}(v_\phi B_z - v_z B_\phi) - \frac{\partial}{\partial r}(v_r B_\phi - v_\phi B_r), \tag{21}$$

$$\frac{\partial^2\psi}{\partial z^2}+\frac{1}{r}\frac{\partial}{\partial r}\left(r\frac{\partial\psi}{\partial r}\right)=4\pi G\rho, \tag{22}$$

where the variables have their ordinary meanings. Equation (15) is the continuity equation; equations (16), (17) and (18) are the equations of motion. The induction equations for the poloidal magnetic fields are equations (19) and (20) and for the toroidal magnetic field is equation (21). The last equation (22) is the Poisson equation.

The MHD equations were solved using van Leer (1977)'s monotonic interpolation and the constrained transport method by Evans & Hawley (1988) with the method of characteristics (MOC) modified by Stone & Norman (1992). This code is based on a hydro-code written from scratch by the author (Tomisaka & Bregman 1993) referring to Norman & Winkler (1986). This is similar to ZEUS2D which is distributed from NCSA. To ensure the specific angular momentum $\rho r v_\phi$ and the toroidal magnetic fields B_ϕ are convected similar to the density, advections of such values are calculated using the consistent advection which is first pointed out by Norman, Wilson, & Barton (1980). We rewrote the advection terms of equations (18) and (21) as

$$\frac{\partial B_\phi}{\partial t} = -\frac{\partial}{\partial z}\left[\left(\frac{B_\phi}{\rho}\right)(\rho v_z)\right]-\frac{\partial}{\partial r}\left[\left(\frac{B_\phi}{\rho}\right)(\rho v_r)\right], \tag{23a}$$

$$\frac{\partial \rho r v_\phi}{\partial t} = -\frac{\partial}{\partial z}\left[(r v_\phi)(\rho v_z)\right]-\frac{1}{r}\frac{\partial}{\partial r}r\left[(r v_\phi)(\rho v_r)\right]. \tag{23b}$$

To evaluate the right-hand-side of equations (18) and (21), we chose the same numerical mass flux $\rho\mathbf{v}$ used in equations (15) and (16) and multiplied B_ϕ/ρ and $r v_\phi$ to the mass flux to get numerical fluxes for the angular momentum density and the toroidal magnetic fields. To solve the Poisson equation (22), we adopted MILUCGS [modified incomplete LU decomposition preconditioned conjugate gradient squared method: Meijerink & van der Vorst (1977); Gustafsson (1978)].

The gravitational contraction proceeds in a significantly non-homologous way. To see the early phase evolution, we have to cover spatially wide region. On the other hand, to see the late phase evolution, high spatial resolution is needed especially near the central compact object. These demands are conflicting with each other. To overcome the difficulty, we adopt the nested grid method (Berger & Oliger 1984; Berger & Colella 1989), similar to our previous series of papers which treated the cloud collapse (Tomisaka 1996, 1998, 2000). In this method, a number of levels of grids with different spacings are prepared; finer grids cover the central high-density portion and the coarser ones cover the cloud as a whole. The grids are named as L0 (the coarsest), L1, L2, ... and the grid spacing of Ln is chosen equal to a half of that of L$n-1$, that is, the grid spacing of Ln is equal to $\Delta z_n=\Delta z_0 2^{-n}$ and $\Delta r_n=\Delta r_0 2^{-n}$. The L0 grid covers the region $-\lambda_{\rm max}/2\le z\le\lambda_{\rm max}/2$ and $0\le r\le\lambda_{\rm max}$.

In the nested grid method, a true boundary condition is applied only to the outer boundary of the coarsest grid L0, on which we adopted the fixed boundary condition at $r = \lambda_{\rm max}$ and the periodic boundary condition at $z = \pm\lambda_{\rm max}/2$. Adopting the periodic boundary condition means that mass and angular momentum are not removed from the system through the upper and lower boundaries. Even if an outflow is ejected and the Alfvén wave generated by the rotational motions propagates, as long as these do not reach the boundaries the results do not suffer from the boundary condition. This is true for all the models we calculated. The code has been tested comparing the results obtained with and without the nested grid technique [for detail see Tomisaka (1996)]. The the most unstable growth rates of perturbations are slightly different ($\simeq 8\%$): $\rho_c = 10^4\rho_s$ was attained at $t = 1.25\tau_{\rm ff}$ for without nested grid (but using relatively large number of grid points 400×400), but at $t = 1.351\tau_{\rm ff}$ in the calculation with the nested grid method. This is mainly due to the fact the eigen-function of the most unstable mode is as wide as the whole size of the numerical box and this mode is represented better by a simple calculation with a large number of zones (400×400) rather than the L0 grid (64×64) of the present scheme. However, after the perturbation has grown to be non-linear, the growth rate agrees well.

As another test, we calculated the evolution of a model (model A) using a set-up in which the number of grid points in one level is increased to 128×128, while the number of levels is unchanged. This gives twice higher spatial resolutions than models which will be shown in the next section. Comparing these two, as is expected, it is found that the time necessary to form the core ($\rho = \rho_{\rm A}$) is slightly different; the calculation with lower resolutions (64×64) gives longer time-scale for core formation ($t_c \simeq 0.7219\tau_{\rm ff}$) than that with higher resolutions (128×128; $t_c \simeq 0.7097\tau_{\rm ff}$), which is consistent with the result of the former test. However, the evolutions after the core formation are the same for two calculations, if we use the time after the core formation epoch, $t - t_c$, instead of t itself. This shows us that the 64×64 grid points in each level are sufficient to discuss the evolution of molecular cloud cores to form stars, if we employ the nested grid technique.

3. Results

3.1. Dynamical Contraction

In Model A, we calculated the evolution with $\alpha = 1$, $\Omega_0 = 5$, $F = 100$, and $\rho_s = 10^2{\rm H_2\,cm^{-3}}$. We summarized the adopted parameters in Table 2. Similar to the *non-rotational* magnetized cloud [see Figs. 2b and 2c of Tomisaka (1996)], the cylindrical cloud fragments into prolate spheroidal shape whose wavelength is equal to $\lambda_{\rm max}$. This prolate spheroidal shape coincides with the structure expected from the linear stability analysis by

Matsumoto, Hanawa, & Nakamura (1994). Next, this density enhanced region begins to contract along the major axis of the cylindrical cloud, since the magnetic fields are assumed to run parallelly to the major axis. Finally it forms a contracting disk (pseudo-disk) perpendicular to the magnetic field lines [Fig. 2d of Tomisaka (1996)]. The snapshot at this stage is shown in Figure 1. Using the conversion factors from nondimensional to dimensional quantities shown in Table1, the epoch $t = 0.6066\tau_{\rm ff}$ corresponds to $1.06{\rm Myr}(\rho_s/10^2{\rm H_2\ cm^{-3}})^{-1/2}$ from the beginning of calculation. Respective panels of Figure 1 have different spatial coverages. Figure 1a, which shows L1, represents a global structure of the contracting disk extending horizontally which is perpendicular to the magnetic field lines. At this epoch, the central density reaches $\rho_c \simeq 10^{8.44}\rho_s$[1]. The figure clearly shows that the cloud continues to collapse. This means that the centrifugal force cannot sustain the cloud collapse. The spatial resolution of L1 is so limited that there seems no internal structures in the contracting disk. However, L5 which has 16 times finer resolution than L1 shows that outward-facing shock fronts extend parallel to the r-direction. Fronts near $z \simeq \pm 0.02H$ are the fast-mode MHD shock fronts, because the magnetic fields bend toward the front passing the shock front. We can see another density jump near $z \sim 0.01H$ (hereafter we will omit the sign $\pm$ and mention the upper half of each figure since the structure is symmetric).

The shock fronts formed parallel to the disk are known in a contracting non-magnetized rotating isothermal clouds (Norman, Wilson, & Barton 1980; Matsumoto, Hanawa, & Nakamura 1997). These are not due to the rotation; multiple shock fronts are also found in the contracting magnetized cloud without rotation (Nakamura et al. 1999). However, situation becomes a bit complicated in this cloud. In the outer region $z \gtrsim 0.02H$, the magnetic field lines run almost vertically ($B_z \gg B_r$ and B_ϕ). Passing the MHD fast shock, in the intermediate region ($0.01H \lesssim z \lesssim 0.02H$), the radial and toroidal components are amplified and the density increases compared to the outer region. Finally after passing another front near $z \simeq 0.01H$, the toroidal component B_ϕ decreases. That is, since the magnetic field lines deflect departing from the front at the second front, this is a slow MHD shock. The density range represented in this panel is from $10^{2.3}\rho_s = 10^{4.3}(\rho_s/100{\rm H_2\ cm^{-3}}){\rm H_2\ cm^{-3}}$ to $10^{7.3}\rho_s = 10^{9.3}(\rho_s/100{\rm H_2\ cm^{-3}}){\rm H_2\ cm^{-3}}$. It should be noticed that these shocks occurs in the isothermal gas. This phase is called "run-away collapse," in which the central density (ρ_c) increases greatly in a finite time-scale.

Figure 1c shows the structure represented in L10. Almost all the gas in this figure is isothermal. However, a central small part of the contracting disk ($r \lesssim 6 \times 10^{-4}H$ and $|z| \lesssim 1 \times 10^{-4}H$) enters the polytropic regime with a harder equation of state than the isothermal

[1]The central density obtained by L1 is only $\rho_c \simeq 10^{4.94}\rho_s$. However, this is owing to the restriction of the spatial resolution of L1. Using deep levels of grids we can obtain the true central density.

one. At this stage, we can see another density jump where lots of density contour lines are confined locally is forming just outside the polytropic part of the disk. This corresponds to the gas with $\Gamma > 1$ which is seen as a gas $\rho > \rho_{\rm A} = 10^8$ in nondimensional units. This density jump seems to grow into an accretion shock front, since it is known that an accretion shock forms outside the core when the adiabatic core develops (Larson 1969). This is easily understood as follows: the gas with specific heat ratio $\gamma > 4/3$ has a hydrostatic equilibrium irrespective of its mass. The scale-height in the z-direction of the core becomes larger than that of the disk. The gas with a harder equation of state forms a spherical static core. Since we assume the multiple polytropic relation for $\rho > \rho_{\rm A}$ [eq(14)], the core should be called a polytropic core. However, we will call it an adiabatic core, in this paper. This is justified since the core is almost spherical (see §2) and similar to that obtained by radiative hydrodynamical calculations assuming the spherical symmetry (Masunaga & Inutsuka 1999).

Figure 2 shows cross-cut views along two axes (along the disk mid-plane $z = 0$ [panel a] and along the z-axis $r = 0$ [panel b]), which shows how the adiabatic core is formed. The lines with 0.6066 represent the stage shown in Figure 1. At this stage ($t = 0.6066\tau_{\rm ff}$), inflowing gas is almost isothermal ($\rho < \rho_{\rm A}$). In Figure 2a, the radial distributions of the density, the magnetic flux density, and the radial and the toroidal components of velocity are shown. We can see that density and magnetic flux density distributions are approximately expressed by power-laws as $\rho \propto r^{-2}$ and $B_z \propto r^{-1}$ except for the central part. At $t = 0.6067\tau_{\rm ff}$, the density in the core exceeds $10^9\rho_s = 10^{11}(\rho_s/100{\rm H_2\,cm^{-3}}){\rm H_2\,cm^{-3}}$. And at $t = 0.6068\tau_{\rm ff}$, it reaches $10^{10}\rho_s = 10^{12}(\rho_s/100{\rm H_2\,cm^{-3}}){\rm H_2\,cm^{-3}}$. At this stage, a radially outward-facing shock front is seen even inside the disk; infall motion is abruptly decelerated and the density and magnetic flux density are compressed. This shows that a compact core is formed inside the accretion shock front. The central density increases with time and inside $r \lesssim 1.8 \times 10^{-4}H$ polytropic gas ($\rho > \rho_{\rm A}$) distributes. The size of the core is equal to $r \sim 1.9 \times 10^{14}(c_s/190{\rm m\,s^{-1}})(\rho_s 10^2{\rm H_2\,cm^{-3}})^{-1/2}{\rm cm} \sim 13(c_s/190{\rm m\,s^{-1}})(\rho_s 10^2{\rm H_2\,cm^{-3}})^{-1/2}{\rm AU}$. This reduces with time since the mass of the core increases by the effect of continuous accretion.

Before the shock front is formed $t < 0.6067\tau_{\rm ff}$, the radial inflow velocity takes the maximum about $\simeq 2.5c_s$ near $r \simeq 7 \times 10^{-3}H$. For the Larson-Penston self-similar solution for the spherically symmetric dynamical collapse (Larson 1969; Penston 1969), this maximum inflow speed is expected equal to $\simeq 3.28c_s$. On the other hand, it equals to $\simeq 1.736c_s$ for the non-rotating isothermal *disk* (Saigo & Hanawa 1998). Therefore, it is shown that the actual inflow speed ranges between those expected for the spherically symmetric self-similar solution and for the axially symmetric thin disk solution. After the shock front is formed around the core, the inflow velocity takes the maximum just outside the shock front and the maximum speed increases with time. Inflow motion is accelerated toward the shock front.

Similar acceleration is also seen in the toroidal velocity, v_ϕ. Before the core formation the toroidal speed v_ϕ takes the maximum $v_\phi \sim 1.7c_s$ near $r \simeq 2.5\times10^{-3}H$. However, v_ϕ increases toward the accretion shock after the core formation. At $t = 0.6068\tau_{\rm ff}$ it reaches $v_\phi \simeq 3c_s$ (see also Fig.1 of Tomisaka (1998)).

Structure seen in the cross-cut along the z-axis is more complicated (Fig.2b). Two shock fronts mentioned earlier (Fig.1b) correspond to the jumps near $|z| \simeq 0.02H$ and $\simeq 0.005H$[2] At $t = 0.6066\tau_{\rm ff}$, the density and the inflowing velocity distributions have no discontinuities besides these two shock fronts. However, at $t = 0.6067\tau_{\rm ff}$, the inflowing velocity distribution begins to indicate a clear discontinuity near $|z| \simeq 1.5\times10^{-4}H$. This shows that a newly formed shock front is propagating spatially. Comparing two curves of $t = 0.6067\tau_{\rm ff}$ and $t = 0.6068\tau_{\rm ff}$, it is shown that this shock front breaks into two fronts and the inner one ($|z| \simeq 1.5\times10^{-4}H$) is standing still, while the outer one ($|z| \simeq 5\times10^{-4}H$) is propagating outwardly. These two shock fronts are outwardly facing. Thus the inwardly propagation of the inner fronts is due to the infalling gas motion.

Figure 2 indicates that the inflow near the z-axis is accelerated reaching the central core. Further, comparing v_z for two different epochs, for example $t = 0.6067\tau_{\rm ff}$ and $t = 0.6068\tau_{\rm ff}$, we can see the inflow near the z-axis is accelerated with time. This is a natural consequence of the fact that the inflow is essentially controlled by the gravity (free-fall) in the z-direction which is parallel to the magnetic fields and angular momentum vectors. In this case, accretion speed increases reaching the source of the gravity. And accretion speed also increases with time.

3.2. Outflow

Figure 3 illustrates the structure at $t = 0.6069\tau_{\rm ff}$. Although the gas is inflowing both inside and outside of the disk at $t = 0.6067\tau_{\rm ff}$ (Fig.2), at this stage $t = 0.6069\tau_{\rm ff}$ ($\tau = 3.2\times10^{-4}\tau_{\rm ff}$)[3] a prominent outflow is formed outside of the disk. This shows that the flow pattern is completely changed in $\Delta t \simeq 2\times10^{-4}\tau_{\rm ff} \sim 400$yr. The outflow sweeps a sphere with radius of $r \lesssim 1.2\times10^{-3}H$ (Fig.3a). Figure 3b indicates that the gas near the disk surface flows inwardly for $r \gtrsim 2\times10^{-4}H$. However, the direction of the flow is changed upwardly near $r \simeq 2\times10^{-4}H$. Finally this gas is ejected. While the gas flowing near the

[2]The shape of the inner slow MHD shock is concave. On the z-axis it is found near $z \simeq 0.005H$, while departing from the z-axis ($r \gtrsim 0.02H$) it is found near $z \simeq 0.01H$.

[3]t represents the time from the beginning of calculation but $\tau \equiv t - t_c$ represents the time after the core formation. We assumed that the core consists of the gas with density $\rho > \rho_{\rm A}$.

mid-plane of the disk ($|z| \lesssim 1 \times 10^{-5} H$) continues to contract. This is reasonable because the total amount of angular momentum in one magnetic flux tube must be conserved in the axisymmetric ideal MHD simulation; for the outflow gas to get angular momentum, a part of the gas in the same magnetic flux tube has to lose its angular momentum and to fall further. In the acceleration process of the gas, the angular momentum is transferred from the gas near the mid-plane to the gas near the surface of the disk. Considering the angular rotation speed, the angular momentum is transferred from the fast-rotating mid-plane to the slowly rotating surface gas.

From Figures 1c and 3a (both show the structure represented in L10), we can see the magnetic field lines run completely differently comparing before ($\rho_c < \rho_{\rm A}$: Fig.1c) and after ($\rho_c > \rho_{\rm A}$: Fig.3a) the adiabatic core formation. That is, in the isothermal runaway collapse phase (Fig.1c) the magnetic field lines run vertically, in other words, perpendicularly to the pseudo-disk. In contrast, after the adiabatic core is formed, the disk continues to contract and drags the magnetic field lines inwardly. Thus the angle between the magnetic field lines and the disk decreases.

Figure 3b is a close-up view whose spatial resolution is 4-times finer than that of Figure 3a. This panel shows us that the angle between the flow and the disk is about $\simeq 45\,{\rm deg}$. The reason why the outflow begins only after the core formation is related to the angle between the magnetic field lines and the disk, $\theta_{\rm mag}$. Blandford & Peyne (1982) have pointed out that for a cold gas rotating with the Keplerian speed to get angular momentum from the Keplerian disk via infinitely strong magnetic fields, $\theta_{\rm mag}$ must be smaller than a critical value $\theta_{\rm cr} = 60\,{\rm deg}$. This is understood as follows: Consider the gas on a magnetic flux tube. When the magnetic flux tube is rising steeply from the disk as $\theta_{\rm mag} > \theta_{\rm cr}$, the gas has to climb the effective potential well even if it rotates with the same angular speed of the Keplerian disk. On the other hand, when $\theta_{\rm mag} < \theta_{\rm cr}$, gas can escape from the gravitational well by getting angular momentum from the disk, if the gas has the same angular speed of the Keplerian disk. Although the exact value of $\theta_{\rm cr}$ depends on the disk rotation speed and the disk-to-central star mass ratio, small angle is preferable to acceleration. This is known as the magneto-centrifugal acceleration mechanism. Kudoh, Matsumoto, & Shibata (1998) have studied a jet ejected from the Keplerian disk with two-dimensional MHD simulations. Using the effective potential defined as

$$\psi_{\rm eff} = \psi - \frac{1}{2}\Omega_{\rm F}^2 r^2, \tag{24}$$

they found that the gas is accelerated after passing the local maximum of this effective potential, when they followed the path of a gas element. (Here $\Omega_{\rm F}$ is the angular velocity of the magnetic field line.) It should be noted that this configuration is achieved only after the core formation (Tomisaka 1998).

To explore which force is working to drive the outflow, we calculated the amplitude of respective forces to drive the flow at each grid points: the pressure gradient $-\nabla p$, the magnetic force $(\nabla \times \mathbf{B}) \times \mathbf{B}/4\pi$, and the centrifugal force $\rho v_\phi^2/r\mathbf{e}_r$. And we compare their components parallel to the poloidal magnetic field as

$$F_p = -\nabla p \cdot \frac{\mathbf{B}_p}{|\mathbf{B}_p|}, \tag{25}$$

$$\begin{aligned} F_m &= \frac{(\nabla \times \mathbf{B}) \times \mathbf{B}}{4\pi} \cdot \frac{\mathbf{B}_p}{|\mathbf{B}_p|} & (26) \\ &= -\frac{1}{8\pi r^2} \frac{\mathbf{B}_p}{|\mathbf{B}_p|} \cdot \nabla (rB_\phi)^2, & (27) \end{aligned}$$

(Ustyugova et al. 1999) and

$$F_c = \frac{\rho v_\phi^2}{r} \frac{B_r}{|\mathbf{B}_p|}. \tag{28}$$

Figure 3c(right) shows the largest force at each grid points. The region filled with asterisks (*) shows the region where the centrifugal force, F_c, dominates over other forces. We will call it region C, which means the centrifugal force-dominated region. An outflow region, which can be seen in the flow vectors displayed in the left-half, extending at an angle of $\simeq \pm 45$ degree to the disk around the point P1 $(z, r) \simeq (1 \times 10^{-4}H, 2.5 \times 10^{-4}H)$ completely agrees with this region C. Just radially exterior to this region C, there is a region near the point P2 $(z, r) \simeq (2 \times 10^{-4}H, 3.5 \times 10^{-4}H)$ filled with plus signs (+) where the magnetic force dominates (region M). We can see the strongest outflow coincides with this region M and the above region C. This means that the outflow is driven by the centrifugal force and the magnetic force (the toroidal magnetic pressure gradient). Another fast outflow found near the point P3 $(z, r) \simeq (2 \times 10^{-4}H, 1.8 \times 10^{-4}H)$ seems to be driven by the centrifugal force, since this is occupied with another region C. A magnetic force dominated region (region M) spreads near the z-axis. However, this is an inflow region. At the blank grid points, the thermal pressure gradient is the largest (region T). As a conclusion, it is shown that the gas outflows through the region C and the region M extending from the disk at an angle of $\simeq \pm 45$ degree.

The toroidal-to-poloidal ratio of the magnetic field strength is as small as ~ 0.6 in the disk, that is, the disk is poloidal-dominated. However, in the region where the gas flows outwardly ($z \gtrsim 5 \times 10^{-4}H$), the toroidal component grows and the toroidal-to-poloidal ratio reaches $\gtrsim 5-8$. In the above regions C and M which coincide with the strongest outflow, the toroidal magnetic field dominates over the poloidal one. The coincidence of the acceleration region with the toroidal-dominant region seems to indicate that the toroidal fields play an

important role to accelerate the gas. This coincidence is understood as follows. The toroidal component of the Lorentz force,

$$\begin{aligned} F_\phi &= \frac{1}{c}\left(j_z B_r - j_r B_z\right) \\ &= \frac{1}{4\pi}\left(\frac{1}{r}\frac{\partial r B_\phi}{\partial r}B_r + \frac{\partial B_\phi}{\partial z}B_z\right), \end{aligned} \tag{29}$$

works mainly below this toroidal-dominant region, that is, $z \lesssim 5 \times 10^{-5} H$. This toroidal component F_ϕ accelerates the toroidal velocity v_ϕ and the resultant toroidal motion amplifies the toroidal component of the magnetic fields. The rotational motion has an effect to increase the centrifugal force and forms region C. And the toroidal magnetic field gives a large magnetic pressure gradient. Therefore, it should be concluded that the gas is accelerated by the centrifugal force and the toroidal magnetic pressure gradient, both of which are driven by the rotational motion of the disk. Outflow speed exceeds the sound speed and the fastest speed reaches $v_{\rm out} \simeq 7.5 c_s$ at this time. This increases with time.

3.3. Effect of the Hardness of the Polytropic Gas

Although the outflow seems to continue, the further evolution is hard to study, because the time-scale (the free-fall time-scale at the central core) becomes shorter and shorter. Therefore, we study model AH with a constant polytropic exponent larger than that of model A. In models AH1 (Fig.4a) and AH2 (Fig.4b), the polytropic exponents are chosen $\Gamma = 2$ and $\Gamma = 5/3$, respectively, for $\rho > \rho_{\rm A}$. (Models whose name have "H" have simple polytropic relation with $\Gamma = 2$ or $\Gamma = 5/3$ for $\rho > \rho_{\rm A}$.) Due to the hard polytropic exponents, the size of the adiabatic core, whose surface is determined by the jump in v_r, becomes large; for example at $t = 0.6069\tau_{\rm ff}$ the size is equal to $r_{\rm c} \simeq 4 \times 10^{-4} H$ for model AH1 and $r_{\rm c} \simeq 3 \times 10^{-4} H$ for model AH2 while it is equal to $r_{\rm c} \simeq 1.5 \times 10^{-4} H$ for model A. Similar to model A, just outside the core, outflow begins to be accelerated. The region swept by the outflow expands and the surface which separates the inflow and the outflow forms another MHD shock front. And the expansion of the front is very similar to that of model A (the front reaches $z \simeq 1 \times 10^{-4} H$ at this time, which is similar to model A).

To see the similarity in more detail, we calculated the mass of the core

$$M_{\rm core} \equiv \int_{\rho > \rho_{\rm A}} \rho dV, \tag{30}$$

for models A, AH1, and AH2. These are equal to $0.1407 c_s^3/(4\pi G)^{3/2}\rho_s^{1/2}$, $0.1504 c_s^3/(4\pi G)^{3/2}\rho_s^{1/2}$, and $0.1450 c_s^3/(4\pi G)^{3/2}\rho_s^{1/2}$ at the time $t = 0.6069\tau_{\rm ff}$ ($\tau = 3.2\times10^{-4}\tau_{\rm ff}$) for models A, AH1 and

AH2, respectively. At later epoch $t = 0.6085\tau_{\rm ff}$ ($\tau = 2\times10^{-3}\tau_{\rm ff} \simeq 3200(\rho_s/10^2{\rm H_2\,cm^{-3}})^{-1/2}{\rm yr}$), $M_{\rm core} \simeq 0.4697c_s^3/(4\pi G)^{3/2}\rho_s^{1/2} \simeq 0.11(c_s/190{\rm m\,s^{-1}})^3(\rho_s/10^2{\rm H_2\,cm^{-3}})^{-1/2}M_\odot$ (model AH1) and $M_{\rm core} \simeq 0.4104c_s^3/(4\pi G)^{3/2}\rho_s^{1/2} \simeq 0.09(c_s/190{\rm m\,s^{-1}})^3(\rho_s/10^2{\rm H_2\,cm^{-3}})^{-1/2}M_\odot$ (model AH2). From these results, it is shown that the core mass increases with time due to the continuous accretion and the mass does not depend on the exact equation of state in the core. This is understood as follows: the core mass is determined by the accretion rate of the *isothermal gas* which is independent from the polytropic exponent Γ in the core.

The gravity by the core has an effect on the outer inflow and outflow. Since the effect depends only on its mass, the difference in the polytropic exponents of the core does not play an important role for the inflow and outflow. Therefore, we will study this model AH to see a long time evolution of the outflow.

In Figure 4c, a snapshot at $t = 0.6105\tau_{\rm ff}$ ($\tau = 4\times10^{-3}\tau_{\rm ff} \simeq 7000(\rho_s/10^2{\rm H_2\,cm^{-3}})^{-1/2}{\rm yr}$) is plotted for model AH1. Comparing this with Figure 1b for model A (both have the same resolution but for different epochs), it is shown that the shock front which separates the inflow and the outflow passed the slow-mode MHD shock front near $z \simeq 0.01H$ and has just reached the outer fast-mode shock front near $z \simeq 0.02H$. The evolution of model AH2 is essentially the same. The maximum speed of the outflow reaches $\sim 8c_s \sim 2(c_s/0.2{\rm km\,s^{-1}}){\rm km\,s^{-1}}$. This maximum speed seems smaller than that observed in the molecular outflow. Since the mass accumulated in the core is only equal to $\sim 0.1(c_s/190{\rm m\,s^{-1}})^3(\rho_s/100{\rm H_2\,cm^{-3}})^{-1/2}M_\odot$, the outflow speed seems to be much faster than this value, when the mass has grown to that of a typical T Tauri star. Figure 3b indicates the outflow is accelerated near the core and the opening angle of the outflow in this region is wide. However, departing from the acceleration region the flow changes its direction toward the z-axis. Figure 4c shows that the opening angle decreases as the outflow proceeds. This indicates the flow is collimated.

3.4. Effect of the Initial Rotation Speed

To see the effect of the initial rotation speed of the cylindrical cloud, we compare models AH1 ($\Omega_0 = 5\tau_{\rm ff}^{-1}$), BH ($\Omega_0 = 1\tau_{\rm ff}^{-1}$), and CH ($\Omega_0 = 0.2\tau_{\rm ff}^{-1}$). These models have the same magnetic field strength, α. In panels (a-c) of Figure 5, the structures at the final epoch of the isothermal run-away collapse phase are plotted for respective models. Models BH and CH indicate no prominent discontinuity in L6 (Figs. 5b and c), while model AH1 has several shock fronts as described in §3.1. However, in L10 (not shown), there are discontinuities near $z \simeq 6\times10^{-4}H$ (model BH) and $z \simeq 5\times10^{-4}H$ (model CH) as well as in model AH1 ($z \simeq 1\times10^{-4}H$). Comparing panels (b) and (c), distributions of the density and magnetic field lines are similar each other. This indicates that the evolution in the isothermal phase

is slightly dependent on the initial angular momentum if $\Omega_0 \lesssim 1 \times \tau_{\rm ff}^{-1}$. This seems to corresponds to the fact that evolutions of the run-away collapse phase with different initial conditions converge each other to a self-similar solution (Nakamura et al. 1999).

Figures 5d-f show the structure at the age $\tau = 4.5 \times 10^{-3}\tau_{\rm ff}$ after the core formation. In all models the outflows are formed. However, the size of the region swept by the outflow is different for each model. With increasing Ω_0, more energetic outflow is driven. From the velocity vectors, it is shown that model AH1 (Fig.6d) forms a bit more collimated outflow than models BH and CH (Figs.6e and f). This seems to correspond to the differences in density distribution and magnetic field configuration. That is, in model AH1 (also A and AH2) there is a relatively thick disk seen in L6 which is bounded by the shock fronts. This thick disk seems to confine the outflowing gas in model AH1. While, in models BH and CH the disk is relatively thin, which seems to make the flow isotropic. Further, the opening angle of the magnetic field lines in models BH and CH is larger than that of model AH1. This causes the flow also open.

Difference between models BH and CH comes from the fact that the epochs when outflows begin are different. Since the initial rotation speed in model BH is five-times larger than that of model CH, in model BH the outflow begins earlier than model CH. When $\tau \simeq 6 \times 10^{-3}\tau_{\rm ff}$ has passed, however, even in model CH the top of the outflow reaches $z \simeq 0.02H$ and the structure looks very similar to model BH at $\tau \simeq 4.5 \times 10^{-3}\tau_{\rm ff}$ (Fig.5e).

At the epoch when the snapshots of Figures 5d-f are taken ($\tau = 4.5 \times 10^{-3}\tau_{\rm ff} \simeq 8 \times 10^3[\rho_s/10^2{\rm H_2\,cm^{-3}}]^{-1/2}$yr), the mass in the adiabatic core reaches $M_{\rm core} \simeq 0.667c_s^3/(4\pi G)^{3/2}\rho_s^{1/2}$ (model AH1), $\simeq 1.311c_s^3/(4\pi G)^{3/2}\rho_s^{1/2}$ (model BH), and $\simeq 1.469c_s^3/(4\pi G)^{3/2}\rho_s^{1/2}$ (model CH). The instantaneous rate of mass accretion to the adiabatic core for each model attains $\dot{M}_{\rm acc} \equiv dM_{\rm core}/dt \simeq 110c_s^3/(4\pi G)$ (model AH1), $\simeq 180c_s^3/(4\pi G)$ (model BH), and $\simeq 220c_s^3/(4\pi G)$ (model CH), respectively. Therefore, the core mass is approximately proportional to the mass accretion rate and the mass accretion rate is larger for models with smaller angular rotation speed Ω_0.

Accretion rate expected from the inside-out collapse model (Shu 1977) is equal to $0.975c_s^3/G = 12.25c_s^3/(4\pi G)$. Therefore, the accretion rates calculated here are $9-18$ times larger than that expected by the inside-out collapse model. While, Whitworth & Summers (1985) obtained another self-similar solution which expresses the evolution after the core formation before which the Larson-Penston self-similar solution is valid for the run-away collapse. Their solution expects the accretion rate of $\simeq 47c_s^3/G = 590c_s^3/(4\pi G)$. The observed accretion rates are smaller than that of Whitworth & Summers (1985).

Consider the reason why the mass of the core decreases with increasing Ω_0. Since the

gas is supplied to the core mainly through the disk, we will consider the mass inflow/outflow transport in the disk. The gas disk can be divided into three regions. Outermost region is occupied with isothermal gas and the gas is contracting or inflowing (pseudo-disk). Therefore the inflow mass rate $(\dot{M}_{\rm in})_{\rm outermost} > 0$ and the outflow mass rate $(\dot{M}_{\rm out})_{\rm outermost} = 0$ in this outermost region. Inside of this region, outflow is generated, although a large part of the gas is still inflowing. Therefore in this middle region, the inflow rate is smaller than that of the outermost region, $(\dot{M}_{\rm in})_{\rm middle} \lesssim (\dot{M}_{\rm in})_{\rm outermost} \simeq (\dot{M}_{\rm in})_{\rm middle} + (\dot{M}_{\rm out})_{\rm middle}$, and the excess mass is transported to the outflow, $(\dot{M}_{\rm out})_{\rm middle} > 0$. Innermost is the adiabatic core. Since the mass accretion rate to the core is equal to the net mass inflow rate from the middle region, $\dot{M}_{\rm acc} \simeq (\dot{M}_{\rm in})_{\rm middle}$.

Mass inflow driven by the self-gravity becomes more important in a model with small Ω_0 in which the self-gravity is ineffectively counterbalanced with the centrifugal force. Therefore $(\dot{M}_{\rm in})_{\rm outermost}$ becomes larger for a slow rotator. This is the first effect of the rotation.

Furthermore, the outflow brings away appreciable amount of gas. As mentioned previously, the outflow is strongly generated in the fast rotator. Thus, the mass outflow rate increases with increasing Ω_0 as $(\dot{M}_{\rm out})_{\rm middle} \sim 80 c_s^3/(4\pi G)$ (model AH1), $\sim 20 c_s^3/(4\pi G)$ (model BH), and $\sim 10 c_s^3/(4\pi G)$ (model CH). As a result, increasing Ω_0, the portion of outflow gas to the inflow gas $(\dot{M}_{\rm out})_{\rm middle}/(\dot{M}_{\rm in})_{\rm middle}$ becomes large as $\sim 40\%$ for model AH1, compared with $\sim 10\%$ for model BH and $\lesssim 5\%$ for model CH. These two effects works cooperatively to reduce the mass accretion rate $\dot{M}_{\rm acc} \simeq (\dot{M}_{\rm in})_{\rm middle}$ to the core for the cloud with a large Ω_0.

The maximum outflow speed realized in respective figures are equal to $V_{\rm max} \simeq 9.3 c_s$ (model AH1), $6.4 c_s$ (model BH), and $3.2 c_s$ (model CH). Since the outflow is accelerated by the effect of the toroidal magnetic fields which are generated by the rotation motion, this $V_{\rm max}$ increases with increasing Ω_0.

As shown in Tomisaka (2000), since the excess angular momentum of the inflowing gas is effectively removed by the outflow, the total angular momentum of the first core which is defined as a gas with $\rho > \rho_{\rm A}$ is equal to $j_{\rm core} \simeq 9.2 \times 10^{-5} c_s H$ contained in the mass of $M_{\rm core} = 0.67 c_s^3/(4\pi G)^{3/2} \rho_s^{1/2}$ (model AH1), $\simeq 2.5 \times 10^{-6} c_s H$ in $M_{\rm core} = 1.31 c_s^3/(4\pi G)^{3/2} \rho_s^{1/2}$ (model BH), and $\simeq 7.4 \times 10^{-6} c_s H$ in $M_{\rm core} = 1.47 c_s^3/(4\pi G)^{3/2} \rho_s^{1/2}$ (model CH). The total angular momenta contained in the first cores with $M_{\rm core}$ are only 1.1%, 0.07%, and 0.9% of the initial ones for respective models.

3.5. Effect of the Magnetic Field Strength

To see the effect of the magnetic field strength, we compare models NH, BH, DH, and EH in which we took $\alpha = 0$, 1, 0.1, and 0.01.

3.5.1. Model without Magnetic Fields

Model NH has no magnetic fields. In Figure 6a, a snapshot at $t = 0.6977\tau_{\rm ff}$ captured by L8 is shown for this model. At this stage, whole the cloud is in the isothermal regime and the disk experiences the run-away collapse even if the centrifugal force may work to support the cloud. This confirms the earlier results obtained in 1980's by Norman, Wilson, & Barton (1980) and Narita, Hayashi, & Miyama (1984). The physical reason why the centrifugal force does not stop the contraction in the isothermal run-away collapse phase is explained in Hayashi (1980) as follows: Due to the the centrifugal force, the mass contained in the Jeans scale ($\sim c_s/(G\rho_c)^{1/2}$) from the center is *decreasing* throughout the collapse. In this sense the centrifugal force does work! Only a small part of the cloud that resides near the center becomes high-density. But, the contraction itself continues and the central density rises greatly in a finite time-scale, as long as the isothermal equation of state is valid.

Similar to the previous magnetized models, after the polytrope becomes hard $\Gamma > 1$ a small adiabatic core is formed first. Since there is no magnetic field, the magnetic braking does not work, however, in this model. Therefore, gas accreting on the core must have a relatively large angular momentum in contrast to the magnetized model. As a result, a centrifugally-balanced ring forms by the gas which accreted on the adiabatic core. The specific angular momentum of the gas increases with the distance from the center. Since the specific angular momentum ($j \equiv rv_\phi$) of newly accreted matter increases further with time, the radius of the centrifugal ring grows radially. Another snapshot in panel (b) at $t = 0.7011\tau_{\rm ff}$ ($\tau \simeq 3.4 \times 10^{-3}\tau_{\rm ff}$) shows the ring clearly. The ring seems unstable for non-axisymmetric perturbations. This may form a spiral structure similar to that found by Klein et al. (1999). However this is beyond the scope of this paper. Therefore, it is concluded that a rotating but non-magnetic cloud leads to a rotating ring after the core formation.

3.5.2. Models with Magnetic Fields

To see the effect of the magnetic field strength, in Figure 7 we compare models BH ($\alpha = 1$), DH($\alpha = 0.1$), and EH ($\alpha = 0.01$). All models have the same initial rotation speed $\Omega_0 = 1$, and the polytropic exponent $\Gamma = 2$. In panels (a)-(c), the structures at the

core-formation epoch are plotted. Comparing these with each other, it is shown that in model BH ($\alpha = 1$) a flare-up disk is formed whose isodensity lines are departing from the disk mid-plane with leaving from the center. Decreasing the initial magnetic field strength from model BH to model EH, the shape of dense part of the disk becomes rounder. Similar effect is already reported for non-rotating magnetized cloud collapse (Tomisaka 1996), that is, deceasing α the shape of the isothermal contracting disk becomes rounder and finally forms a sphere for $\alpha = 0$.

In panel (d) we plotted a snapshot for model BH at $t = 0.7264\tau_{\rm ff}$ ($\tau = 4.46 \times 10^{-3}\tau_{\rm ff}$) represented in L7. This is the same as illustrated in Figure 5e but for L7 which has twice as fine spatial resolution as Figure 5e. Figure 7d which shows the structure near the root of the outflow indicates that this is very similar to that of model AH1. For example, the outflow leaves from the disk in the direction almost parallel to the disk but it changes its direction to the z-direction. This figure shows that in a time-scale of $\tau \simeq 4.5 \times 10^{-3}\tau_{\rm ff}$, the flow pattern is completely changed from the run-away collapse to the outflow plus continuous inflow in the disk. The outflow gas flows through a region whose shape resembles a capital letter U. The outflow departs from the disk with a wide opening angle but it changes its direction parallelly to the z-axis.

In panel (e), we plotted the structure expected for a model with weaker magnetic fields (model DH: $\alpha = 0.1$ and $\Omega_0 = 1$). The snapshot corresponds to the epoch of $t = 0.7836\tau_{\rm ff}$. This corresponds to $\tau = 4.59 \times 10^{-3}\tau_{\rm ff}$ which is similar to the time-scale between panels (a) and (d). In contrast to the previous model BH, the outflow gas is observed to form a sphere and the magnetic field lines are folded inside this sphere. The magnetic field lines are folded by the pinch or the hoop stress by the toroidal magnetic field. The toroidal magnetic field component is the strongest in the region where the adjacent poloidal magnetic field lines are running in the opposite directions. For example, the regions around $(z, r) \sim (0.003H, 0.004H)$ and $(z, r) \sim (0.003H, 0.006H)$ in Figure 7e.

In this model, the initial poloidal magnetic fields are weak compared to the previous model BH. Therefore, rotation motion amplifies the toroidal fields and their strength surpasses easily that of the poloidal ones. Thus, the hoop stress by the toroidal field pinches efficiently the poloidal magnetic field lines. In the outflow acceleration region, the toroidal component is predominant over the poloidal one. Magnetic field lines are pinched locally and folded. As a result, a spherical magnetic bubble is formed in this process, in which the toroidal magnetic field is predominant.

Toroidal component of the magnetic fields is continuously generated by the twisting motion driven by the disk rotation. The disk angular momentum is transferred by this process. As a result, we do not see any rings which are supported by the centrifugal force.

For the model with extremely weak field, we calculated model EH ($\alpha = 0.01$ and $\Omega_0 = 1$). In panel (f), we plotted the snapshot at $t = 0.7830\tau_{\rm ff}$ ($\tau = 4.53 \times 10^{-3}\tau_{\rm ff}$). Density distribution and magnetic field configuration show that the flow in the magnetic bubble becomes more complicated or turbulent in this model. Figure 7f shows that the magnetic field lines and flow velocities of model EH have spatially smaller-scale variations than model DH in panel (e). The shape of the bubble is more elongated than that formed in model DH. Distribution of toroidal field lines seem not to show any systematic pattern inside the bubble. Size of the bubble both in the z- and r-directions are smaller than those of models BH and DH. Thus, it is concluded that the size of the outflow region increases with increasing the magnetic field strength α. Comparing these three models, it is shown that there are at least two types of outflows. That is, a laminar U-type flow in which fast moving gas flows through a region whose shape resembles a capital letter U and a turbulent outflow in which the magnetic fields and the velocity change their directions in a small scale. For weak poloidal magnetic fields, the global flow pattern of the outflow looks like a capital letter I. Therefore, it is concluded that there are two patters of outflows: the U-type flow for $\alpha \simeq 1$ and the I-type flow for $\alpha \ll 1$.

Similar plots as Figure 3c are shown in panels (g) and (h) for models DH and EH, respectively. The centrifugal force-dominated region (region C) which is indicated by the '*' signs is found mainly near the disk. While, departing from the disk, the magnetic force-dominated region (region M) indicated by the '+' signs becomes to distribute predominately. This shows us that to launch the gas from the disk both the centrifugal force and the toroidal magnetic field gradient work. While, the toroidal magnetic field gradient has an important role to expand the bubble. That is, the magnetic energy stored inside the I-flow drives the outflow motion. It should be noticed that this is completely different from Figure 3c with strong magnetic fields, in which regions M and C form a line and along the line gas seems to be accelerated.

Calculating the plasma $\beta \equiv c_s^2\rho/[(B_z^2 + B_r^2 + B_\phi^2)/8\pi]$, the magnetic bubble or the I-type outflow shows $\beta < 1$, while the outer pseudo-disk shows $10 < \beta < 100$ for model EH. This value is larger than that of model BH, which shows $\beta < 0.1$ in the outflow and $1 \lesssim \beta \lesssim 10$ in the disk. This difference comes from the fact that the initial magnetic field is weak $\alpha = 0.01$ for model EH. However, it should be noticed that even the initial magnetic field is weak the magnetic field is amplified greatly from the seed field in the outflow region. A quarter of the outflow in volume is occupied with a gas of $\beta < 0.1$, which indicates that the magnetic field is important to the dynamics of the outflow. On the other hand, considering the poloidal magnetic field, the magnetic field lines are folded almost vertically in the magnetic bubble. In other words, a large part of the bubble is occupied with poloidal magnetic field lines dominated by B_z over B_r. This configuration is disadvantageous to the magneto-centrifugal

acceleration mechanism (§3.2). In this case, the magnetic force (the magnetic pressure gradient) seems to accelerate the gas.

The core masses accumulated in $\tau \sim 4.5 \times 10^{-3}\tau_{\rm ff}$ are equal to $1.3c_s^3/(4\pi G)^{3/2}\rho_s^{1/2}$ for model BH, $0.87c_s^3/(4\pi G)^{3/2}\rho_s^{1/2}$ for model DH, and $0.65c_s^3/(4\pi G)^{3/2}\rho_s^{1/2}$ for model EH. This shows that the mass accretion rate, $\dot{M}_{\rm acc}$, is an increasing function of the initial magnetic field strength, α. This seems strange if we remember $\dot{M}_{\rm acc}$ is an decreasing function of the initial rotation speed, Ω_0, since both α and Ω_0 have the same effect to counterbalance against the self-gravity. This means that the mass inflow rate in the isothermal run-away collapse region, $(\dot{M}_{\rm in})_{\rm outermost}$, increases with increasing α. This seems to come from a number of reasons, that is, the initial cylindrical cloud becomes more massive with increasing α. Another reason is related to the characteristic wave speed in the magnetized medium. That is, the characteristic speed of the fast mode MHD wave is equal to $(c_s^2+B_0^2/4\pi\rho)^{1/2} = c_s(1+\alpha)^{1/2}$ in the case that the wave is propagating perpendicular to the magnetic field lines. This implies that the mass inflow rates are proportional to the cube of the characteristic wave speed as $c_s^3(1+\alpha)^{3/2}$, which leads the accretion rates for these models as BH: DH: EH = 2.83: 1.15: 1.02. This is not inconsistent with the actual values.

4. Discussion

4.1. Evolution to Form the Second Core

In the previous section, we introduced a simple polytrope above the critical density $\rho > \rho_{\rm A}$ except for model A. However, this is an approximation to see a long evolution. In this section, the evolution assuming the multiple polytrope (eq. 14) is shown. Here, a further evolution later than that shown in Figures 1 and 2 is shown. In model R, we used the multiple polytrope to include combined effects such as the dynamical compressional heating, the radiative cooling through the dust thermal emissions, and the energy loss associated with the H_2 dissociation. This corresponds to the continuation of model A but we consider here a more compact cloud as $\rho_s = 10^4{\rm H_2\,cm^{-3}}$. It should be addressed since ρ_s is assumed hundred-times larger than other models, the size scale $H \simeq 1.05\times10^{17}(c_s/190{\rm m\,s^{-1}})(\rho_s/10^4{\rm H_2\,cm^{-3}})^{-1/2}{\rm cm}$ is 10-times smaller than other models with $\rho_s = 10^2{\rm H_2\,cm^{-3}}$.

The evolution up to the first core formation is similar to model A. After the equation of state becomes hard, $\rho > \rho_{\rm A}$, collapse of the core slows down and isothermal gas begins to accrete on to the core. In Figure 8a, we plotted the structure represented in L6 just before the first core formation $t = 0.7201\tau_{\rm ff}$.

Since the accretion continues, the mass of the first core increases with time, which

leads to a quasi-static core collapse. The structure at this stage (at $t = 0.7239\tau_{\rm ff}$ or $\tau = 3.8 \times 10^{-3}\tau_{\rm ff}$) is shown in panel (b). The radius of the first core shown in this panel is equal to $r \sim 3.5 \times 10^{-4} H \simeq 2.45(c_s/190{\rm m\,s^{-1}})(\rho_s/10^4{\rm H_2\,cm^{-3}})^{-1/2}$ AU. The curved boundary of the core is real.[4] This quasistatic contraction phase ends when the central density reaches $\rho_{\rm B}$.

The structure at this stage ($t = 0.724230\tau_{\rm ff}$ [$\tau = 4.132 \times 10^{-3}\tau_{\rm ff}$]) is plotted in panel (c). Comparing this with panel (b), both of which illustrate L12, it is clear that the adiabatic core is shrinking. After that, a second collapse begins. Since the thermal energy is lost by the process of the dissociation of H_2, the equation of state is assumed to be soft ($\gamma \simeq 1.1$) again. In this phase, the flow is very similar to that realized in the isothermal run-away collapse phase ($\rho_c < \rho_{\rm A}$). The similarity comes from the fact that the equations of states for both two phases are soft ($\Gamma \simeq 1$). In panel (d), we plotted the structure represented in L16 at $t = 0.724236\tau_{\rm ff}$ ($\tau = 4.138 \times 10^{-3}\tau_{\rm ff}$), which represents the typical structure in the second collapse phase. It should be realized that the flow pattern of the second collapse is very similar to the first collapse (the isothermal run-away collapse). This continues until the central density exceeds $\rho_c > \rho_{\rm C}$, beyond which another adiabatic core (the second core) is formed shown in panel (e). The size of the second core is equal to $\simeq 1.3 \times 10^{-6} H \sim 2R_\odot(c_s/190{\rm m\,s^{-1}})(\rho_s/10^4{\rm H_2 cm^{-3}})^{-1/2}$. This meets a similar situation when the first adiabatic core is formed, that is, a central part of the gas obeys a harder equation of state and forms a quasistatic core, while the outer part obeys a softer equation of state and continues to collapse. Analogy between the first and the second core leads to an expectation of a bipolar outflow around the second core. In panel (f), it is shown the second outflow is formed around the second core. This is a snapshot of L16 at $t = 0.724237\tau_{\rm ff}$ ($\tau = 4.140 \times 10^{-3}\tau_{\rm ff}$), which resembles the structure seen in Figure 3b.

This model strongly indicates us that there is another kind of outflow accelerated around the second core (the second outflow) besides that formed around the first core (the first outflow). The flow speed of the second outflow, $\sim 50c_s$, is much faster than that of the first outflow. This seems to come from a fact that the outflow occurs in circumstances to form a faster outflow, for example, the thermal speed near the second core is much faster and the local gravitational potential is much deeper compared with the site where the first outflow is formed. Since the time span of the simulation shown here is restricted, we can not trace

[4]To explore the reason why the surface of the core becomes wavy, we plotted the angular rotation speed, which varies in the polytropic core. The ridge is formed mainly by fast-rotating gas, while the trough corresponds to slowly rotating gas. The angular momentum of the core is dependent upon the efficiency of the angular momentum transport to the outflow. That is, core-gas in a magnetic flux tube from which the strong outflow blows has a small angular momentum. Such a gas even shows the counter rotation.

the evolution further. However, the simulation predicts that at least two different outflows are formed each of which is related to different types of adiabatic cores. Since the flow speed of the second outflow is much faster than that of the first outflow, the respective outflows correspond to the molecular bipolar outflow (the first outflow) and the fast neutral wind or the optical jets (the second outflow). The radial size of the outflow is approximately equal to $\sim 2\times10^{-5}H \sim 2.1\times10^{12}(c_s/190\mathrm{m\,s^{-1}})(\rho_s/10^4\mathrm{H_2cm^{-3}})^{-1/2}$cm (=0.14 AU or $30R_\odot$). This indicates that optical jets are found inside molecular bipolar outflows.

In model R, we assumed the ideal magnetohydrodynamics. However, the ionization fraction of high-density gas is quite low and the electric conductivity decreases as collapse proceeds. Calculation of ionization equilibrium (Nakano & Umebayashi 1986) shows us that after $n_{\rm H} \gtrsim 10^{12}\mathrm{cm^{-3}}$ charged grains are more abundant than ions, and become carriers of the electric currents. Since the mass-to-charge ratio of grains is much larger than that of ions, the electric conductivity decreases greatly and the magnetic field decays mainly through the Joule dissipation. Therefore, in the late phase of the first core (quasistatic contraction), the magnetic field in the core decreases its strength till the field configuration becomes force-free. After the dissociation of H_2 begins, the temperature of the central region is enough high to achieve the thermal ionization of metals. Thus, in the second collapse phase, coupling of magnetic fields is recovered. From these, the ideal MHD is consistent in the first and the second collapse phases. However, the magnetic flux density at the beginning of the second collapse phases seems to be much weaker than that obtained here. As shown in §3.5.2, when the poloidal magnetic field is weak, the flow pattern is different from the case that the magnetic energy is comparable to the thermal one. Therefore, if the magnetic flux is partly lost from the central part of the first core, a turbulent outflow around the second core seems to be formed similar to Figure 7f.

4.2. Mass Inflow/Outflow Rate

Here in this subsection, mass inflow/outflow rates and linear momentum outflow rates are seen more closely. The outflow mass loss rate through the boundary of each grid level is calculated as

$$\dot{M}_{\rm out}(\mathrm{L}n) = \int_{\text{boundary of L}n} \rho \max[\mathbf{v}\cdot\mathbf{n}, 0] dS, \tag{31}$$

where $\mathbf{n}$ represents the unit vector outwardly normal to the surface. The integrand means that only the outwardly running mass flux is summed up. Similarly, the mass inflow rate is calculated as

$$\dot{M}_{\rm in}(\mathrm{L}n) = \int_{\text{boundary of L}n} \rho \max[-\mathbf{v}\cdot\mathbf{n}, 0] dS. \tag{32}$$

These rates are calculated for respective levels of the nested grid system.

The time variations of mass inflow and outflow rates are illustrated for respective models in Figure 9. The time (horizontal axis) is measured from the epoch of the core formation. Time variations, especially longer time variations, seen in the inflow rates are common for all panels. Just after the core formation, the inflowing mass flux decreases with the distance from the center or from L11 to L6. This means that the inner part of the isothermal collapse region is well expressed by the Larson (1969)-Penston (1969) self-similar solution (Ogino, Tomisaka, & Nakamura 2000) which leads to a mass inflow rate of $47c_s^3/G$; Departing from the center, the approximation of the Larson-Penston solution becomes worse and the inflow rate decreases. At $\tau \sim 4 \times 10^{-3} \tau_{\rm ff}$ the inflow rates for various surfaces converge to $\simeq 20 c_s^3/G$, although intense outflow reduces the inflow rate below this value.

We will see each model more closely. Mass outflow rate rises in the deeper levels (Ln with larger n) first and this propagates to lower levels (Ln with smaller n). This indicates the outflow region expands outwardly. Comparing models AH1 (panel a), BH (panel b), and CH (panel c), the effects of the initial rotation speed, Ω_0, are apparent.
(1) with increasing Ω_0, the outflow begins earlier.
(2) with increasing Ω_0, the mass outflow rate increases; although the ratio $\dot{M}_{\rm out}/\dot{M}_{\rm in}$ is equal to only $\sim 10\%$ in model CH ($\Omega_0 = 0.2$), in model AH1 ($\Omega_0 = 5$) it attains $\sim 50\%$.

We compare models BH (panel b), DH (panel d), and EH (panel e) to see the effects of the initial magnetic field strength, α. This indicates that with decreasing α (from models BH to DH) the mass outflow rate increases. However, in model E, in which we assumed extremely weak poloidal magnetic fields, the time variations in the mass inflow and outflow rates are rather chaotic which are lead by the chaotic flow pattern realized in model EH (Fig.7f). Averaging the rates as $< \dot{M} >= \int_0^T \dot{M} dt/T$, the mass outflow rate of model E is $\sim 20 - 40\%$ *smaller* than that of model DH. Considering the disk after rotating at a fixed angle, the disk of model EH can generate weaker toroidal magnetic fields than model DH, since model EH has only weak poloidal (source) magnetic fields. Therefore, it is reasonable that the mass outflow rate in model EH, $< \dot{M}_{\rm out} >$, is smaller than that of model DH.

How about the increase in the mass outflow rare from models BH to DH? This is inconsistent with the above discussion. This increase seems related to the fact that the flow patterns of models BH and DH are different. That is, in model DH a magnetic bubble, in which magnetic field lines are folded and amplified, is formed and the bubble expands. In contrast, in model BH, the gas is flowing outward along specific magnetic field lines and outflowing gas moves through a region which looks like a capital letter U. Mass outflow rate seems larger in the magnetic bubble type outflow rather than the U-type outflow.

The linear momentum outflow rates are calculated by

$$\left.\frac{dMV}{dt}\right|_{\rm out}({\rm L}n) = \int_{\text{upper and lower boundaries of L}n} \rho v_z \max[\mathbf{v}\cdot\mathbf{n}, 0] dS, \tag{33}$$

where we summed up the outflowing linear momentum in the z-direction through the upper and lower boundaries of Ln. Time variations of momentum outflow rate are shown in Figure 10.

Panels (a), (b), and (c) have a prominent common feature that the momentum outflow rates (dMV/dt) calculated at the boundaries of Ln for $n \leq 7$ are much larger than those of the boundaries of Ln for $n > 7$. This feature is common in models with $\alpha = 1$ (models AH1, AH2, BH, and CH). However, models with weaker magnetic fields do not show this feature. Recall the fact that models AH1, AH2, BH, and CH form the U-shaped outflow and in contrast models DH and EH form the magnetic bubble or the I-type outflow. Difference in the momentum outflow rate seems to be related to the outflow pattern. In the laminar U-shaped outflow, the outflow is ejected with a rather wide opening angle and collimated to the symmetric axis. Since equation (33) counts the momentum passing the upper and lower boundaries, the outflow rate increases after the outflow is collimated and the gas flows parallel to the z-axis. This occurs in the larger scale than L7.

Typical momentum outflow rates for molecular bipolar outflows observed with ^{12}CO($J = 2-1$) (Bontemps et al. 1996) are distributed between $\sim 10^{-4} M_\odot {\rm yr}^{-1}\,{\rm km\,s}^{-1}$ for objects associated with active Class 0 IR sources and $\sim 2\times10^{-6} M_\odot {\rm yr}^{-1}\,{\rm km\,s}^{-1}$ for objects associated with late Class 1 IR sources. This range corresponds to $320c_s^4/G - 6.5c_s^4/G$, respectively, if we assume $c_s = 190{\rm m\,s}^{-1}$. Figure 10 shows us that the momentum outflow rate in the range from $\sim 10c_s^4/G$ to $\sim 40c_s^4/G$ is expected. Thus, the momentum outflow rates for almost all the CO bipolar outflow sources associated with low-mass young stellar objects are explained by our model except for the active early class 0 sources.

Comparing models AH1, BH, and CH, it is shown that the momentum outflow rate increases with Ω_0. Comparing mass outflow and momentum outflow rates, models AH1, BH, and CH indicate that the momentum outflow rate is approximately proportional to the mass outflow rate, which means that the outflow speed is approximately equal irrespective of Ω_0. However, changing α is more complicated. Compare panels (b), (d), and (e). As shown in Figure 9, model DH ($\alpha = 0.1$) shows larger mass outflow rate than model BH ($\alpha = 1$). In contrast, as for the momentum outflow rate, the maximum rate of model BH is larger than that of model DH (Fig.10). This means the outflow speed of model BH ($\alpha = 1$) is faster than model DH ($\alpha = 0.1$). Panel (e) shows that the momentum outflow rate has a chaotic time variation as well as the mass outflow rate (Fig.9e), for model EH, which seems to correspond the turbulent outflow shown in Figure 7f.

Summarizing the effect of changing α,
(1) the mass outflow rate increases with increasing α for $\alpha \lesssim 0.1$ but decreases after $\alpha \gtrsim 0.1$.
(2) the outflow speed is an increasing function of α.
(3) there are distinctly different two types of flow patterns: models with strong magnetic fields lead the U-shape outflow, while the flow becomes turbulent for models with weak magnetic fields.

4.3. Estimates of Angular Momentum

Here, we intend to clarify where the outflow is ejected. In the run-away collapse phase, the rotational motion is relatively unimportant. After the core formation, the rotation motion increases especially around the first core. This occurs near the centrifugal radius, which is defined for a gas with specific angular momentum j as

$$R_{\rm c} = c_{\rm c}\frac{j^2}{GM}, \tag{34}$$

where M denotes the mass inside the radius $R_{\rm c}$ and $c_{\rm c}$ represents a numerical factor of the order of unity. Considering a self-similar solution for the run-away collapse phase (Saigo & Hanawa 1998), the specific angular momentum j is proportional to M. This is confirmed by numerical calculations as the mass and the specific angular momentum are proportional to each other (see Fig.2 of Tomisaka (2000)). This is valid only at the core formation epoch and the core loses its angular momentum after the core formation. Further a uniform-density cylinder which is rotating with a uniform rotation speed ω has a j-distribution proportional to M. Assuming $j = qGM/c_s$ (q is a numerical factor), the centrifugal radius is written

$$R_{\rm c} = c_{\rm c}\frac{q^2 GM}{c_s}. \tag{35}$$

As shown in §3, the angular momentum is redistributed in one magnetic flux tube, after the core is formed and the outflow begins to flow. That is, gas near the disk surface obtains a large amount of the specific angular momentum but that near the disk mid-plane loses the angular momentum. If the gas near the disk surface has the angular momentum of $j_+ > j$ in consequence of the angular momentum redistribution, the condition that the effective potential at the centrifugal radius

$$\Phi(R_{\rm c}) = -\frac{GM}{R_{\rm c}} + \frac{j_+^2}{2R_{\rm c}^2} \tag{36}$$

is larger than or equal to zero leads to a minimum angular momentum of

$$j_+ \geq (2c_{\rm c})^{1/2} j, \tag{37}$$

above which the gas with the specific angular momentum may escape from the gravitational well. Since the angular momentum transfer occurs mainly after the core formation, the specific angular momentum j expected for a magnetized cloud is comparable to that of the nonmagnetized one (j) *at the core formation epoch*. After the core formation epoch, due to the angular momentum re-distribution j of the gas near the disk surface increases. Equation (37) shows us that if the specific angular momentum of such a gas exceeds $(2c_{\rm c})^{1/2}j$, the excess centrifugal force can drive the gas outwardly. The fact that the factor $(2c_{\rm c})^{1/2} \simeq 1$ is not too large seems to ensure the ejection of the outflow by this mechanism.

5. Summary

We have explored the evolution of a magnetized interstellar cloud rotating around the symmetric axis. Following the change in the equation of state of the interstellar gas (Tohline 1982), the cloud experiences several phases before going to a star, that is, the isothermal run-away collapse, the slowly contracting core composed of the molecular hydrogen (the first core), the second run-away collapse in the high-density gas where the dissociation of hydrogen molecules proceeds, and finally the second core which is made up of the atomic hydrogen. The magnetized cloud forms pseudo-disks in which the first and the second run-away collapses occur. The pseudo-disks are threaded by the magnetic field lines running perpendicularly to the disk. In the pseudo-disk, a number of fast- and slow-mode MHD shock pairs are formed whose wave fronts are extending parallelly to the disk. Just after the first core is formed at the center, an accretion shock front appears which surrounds the core, through which the supersonic inflow motion is decelerated. While the first and second cores are slowly contacting, the outer pseudo-disks continue to contract. Just outside the accretion shock front, the infall motion is accelerated and thus rotational motion becomes important from the conservation of angular momentum. By the effect of rotational motion, the toroidal magnetic fields and the poloidal electric currents are amplified, which bring a strong magnetic torque. The magnetic torque leads the angular momentum transfer from the mid-plane to the surface of the pseudo-disk. This is actually confirmed by the fact that in the outflow region the centrifugal force and the magnetic pressure gradient of the toroidal magnetic fields are dominant over the thermal pressure gradient. This is the origin of the outflow found in star forming regions. Large-scale bipolar molecular outflows are made outside of the first core, while optical jets and fast neutral winds are expected to be accelerated outside of the second core. Matter losing its excess angular momentum continues to contract further to form a star.

The author would like to thank an anonymous referee who provided useful comments

to improve the paper. This work was supported partially by the Grants-in-Aid (11640231, 10147105) from MEXT (the Ministry of Education, Culture, Sports, Science and Technology). Numerical calculations were carried out by Fujitsu VPP5000 at the Astronomical Data Analysis Center, the National Astronomical Observatory, an inter-university research institute of astronomy operated by MEXT, Japan.

REFERENCES

Basu, S., & Mouschovias, T. Ch. 1994, ApJ, 432, 720

Basu, S., & Mouschovias, T. Ch. 1995, ApJ, 452, 386

Bate, M. R. 1998, ApJ, 508, 95

Bentz, W. 1984, A&A, 139, 378

Berger, M.J. & Colella, P. 1989, J. Comput. Phys., 82, 64

Berger, M.J. & Oliger, J. 1984, J. Comput. Phys., 53, 484

Blandford, R. D., & Peyne, D. G. 1982, MNRAS, 199, 883

Bodenheimer, P. 1995, ARA&A, 33, 199

Bodenheimer, P., Tohline, J. E., & Black, D. C. 1980, ApJ, 242, 209

Bontemps, S., Andre, P., Terebey, S., Cabrit, S. A&A, 311, 858

Boss, A.P. ApJ, 545, L61

Boss, A.P. ApJ, 551, L167

Ciolek, G.E., & Basu, S. 2000, ApJ, 529, 925

Dorfi, E. 1982, A&A, 114, 151

Dorfi, E. 1989, A&A, 225, 507

Evans, C. R., Hawley, J. F. 1988, ApJ, 332, 659

Fiedler, R. A., & Mouschovias, T. Ch. 1992, ApJ, 391, 199

Fiedler, R. A., & Mouschovias, T. Ch. 1993, ApJ, 415, 680

Goodman, A. A., Jones, T. J., Lada, E. A., & Myers, P. C. 1992, ApJ, 399, 108

Goodman, A. A., Jones, T. J., Lada, E. A. & Myers, P. C. 1995, ApJ, 448, 748

Gustafsson, I. 1978, BIT, 18, 142

Hayashi, C. 1980, in "Star Forming Regions," ed. M. Peimbert, & J. Jugaku (Dordrecht: D.Reidel), p.403

Heyer, M. H., et al. 1987, ApJ, 321, 855

Klein, R.I., Fisher, R.T., McKee, C.F., Truelove, J.K. 1999, in "Numerical Astrophysics," ed. S.M. Miyama, K. Tomisaka, & T. Hanawa. (Boston: Kluwer Academic), p.131

Kudoh, T., Matsumoto, R., & Shibata, K. 1998, ApJ, 508, 186

Larson, R.B. 1969, MNRAS, 145, 271

Loren, R.B. 1989, ApJ, 338, 902

Matsumoto, T., Nakamura, F., & Hanawa, T. 1994, PASJ, 46, 243

Matsumoto, T., Nakamura, F., & Hanawa, T. 1997, ApJ, 478, 569

Masunaga, H., & Inutsuka, S. ApJ, 510, 822

Meijerink. J. A., & van der Vorst, H. A. 1977, Math. Comp., 31, 148

Mouschovias, T. Ch., & Morton S. A. 1991, ApJ, 371, 296

Mouschovias, T. Ch., & Morton S. A. 1992, ApJ, 390, 144

Nakamura, F., Matsumoto, T., Hanawa, T. & Tomisaka, K. 1999, ApJ, 510, 274

Nakamura, F., Hanawa, T. & Nakano, T. 1995, ApJ, 444, 770

Nakano, T., Umebayshi, T. 1986, MNRAS, 218, 663

Narita, S., Hayashi, C., & Miyama, S. M. 1984, Prog. Theor. Phys. 72, 1118

Norman, M.L., Wilson, J.R., & Barton, R.T. 1980, ApJ, 239, 968

Norman, M. L. & Winkler, K.-H. A. 1986, in "Astrophysical Radiation Hydrodynamics" ed. K.-H. A. Winkler, & M. L. Norman (Dordrecht: D. Reidel), p.187

Ogino, S., Tomisaka, K., & Nakamura, F. 1999, PASJ, 51, 637

Ohashi, N., Lee, S.W., Wilner, D.J., & Hayashi, M. 2000, ApJ, 518, L41

Penston, M.V. 1969, MNRAS, 144, 425

Phillips, G. L. 1986a, MNRAS, 221, 571

Phillips, G. L. 1986b, MNRAS, 222, 111

Saigo, K. & Hanawa, T. ApJ, 493, 342

Scott, E. H. & Black, D. C. 1980, ApJ, 239, 166

Shu, F.H. 1977, ApJ, 214, 488

Stodółkiewicz, J.S. 1963, Acta Astron., 13, 30

Stone, J. M. & Norman, M. L. ApJS, 80, 753

Tohline, J. E. 1982, Fundamentals of Cosmic Physics, 8, 1

Tomisaka, K. & Bregman, J.N. 1993, PASJ, 45, 513

Tomisaka, K., Ikeuchi, S., & Nakamura T. 1990, ApJ, 362, 202

Tomisaka, K. 1995, ApJ, 438, 226

Tomisaka, K. 1996, PASJ, 48, 701

Tomisaka, K. 1998, ApJ, 502, L163

Tomisaka, K. 2000, ApJ, 528 L41

Truelove, J. K., Klein, R. I., McKee, C. F., Holliman, J. H., II, Howell, L. H., & Greenough, J. A. 1997, ApJ, 489, L179

Truelove, J. K., Klein, R. I., McKee, C. F., Holliman, J. H., II, Howell, L. H., Greenough, J. A., & Woods, D. T. 1998, ApJ, 495, 821

Tsuribe, T., & Inutsuka, S. 1999a, ApJ, 523, L155

Tsuribe, T., & Inutsuka, S. 1999b, ApJ, 526, 307

Ustyugova, G.V., Koldoba, A.V., Romanova, M.M., Chechetkin, V.M., & Lovelace, R.V.E. 1999, ApJ, 516, 221

van Leer, B. 1977, Journal Comput. Phys., 23, 276

Whitworth, A., & Summers, D. 1985, MNRAS, 214, 1

Wood, D. 1982, MNRAS, 199, 331

Table Captions

Table 1: Conversion from the non-dimensional to the physical quantities .

Physical Quantities	Conversion Factors	Physical Values ($\mu = 2.33$)
Velocity	c_s	$190\mathrm{m\,s^{-1}}$
Density	ρ_s	$10^2\mathrm{H_2\,cm^{-3}}$
Length	$c_s/(4\pi G\rho_s)^{1/2} \equiv H$	$0.341(c_s/190\mathrm{m\,s^{-1}})(\rho_s/10^2\mathrm{H_2\,cm^{-3}})^{-1/2}\mathrm{pc}$
Time	$(4\pi G\rho_s)^{-1/2} \equiv \tau_{\rm ff}$	$1.75(\rho_s/10^2\mathrm{H_2\,cm^{-3}})^{-1/2}\mathrm{Myr}$
Mass	$c_s^3/(4\pi G)^{3/2}\rho_s^{1/2}$	$0.227(c_s/190\mathrm{m\,s^{-1}})^3(\rho_s/10^2\mathrm{H_2\,cm^{-3}})^{-1/2}M_\odot$
Mass accretion rate	$c_s^3/4\pi G$	$1.29\times10^{-7}(c_s/190\mathrm{m\,s^{-1}})^3M_\odot\mathrm{yr^{-1}}$
	c_s^3/G[a]	$1.62\times10^{-6}(c_s/190\mathrm{m\,s^{-1}})^3M_\odot\mathrm{yr^{-1}}$
Momentum inflow/outflow rate	$c_s^4/4\pi G$	$2.45\times10^{-8}(c_s/190\mathrm{m\,s^{-1}})^4M_\odot\mathrm{yr^{-1}km\,s^{-1}}$
	c_s^4/G[b]	$3.08\times10^{-7}(c_s/190\mathrm{m\,s^{-1}})^4M_\odot\mathrm{yr^{-1}km\,s^{-1}}$
Magnetic Field	$c_s\rho_s^{1/2}$	$3.75(c_s/190\mathrm{m\,s^{-1}})(\rho_s/10^2\mathrm{H_2\,cm^{-3}})^{1/2}\mu\mathrm{G}$

[a] To meet the conventional normalization, we adopt c_s^3/G in § 4.

[b] To meet the conventional normalization, we adopt c_s^4/G in § 4.

Table 2: Model Parameters.

Model	α	Ω_0	$\rho_{\rm A}$	ρ_s (H_2 cm^{-3})	polytrope
A ...	1	5	10^8	10^2	Realistic
AH1 ...	1	5	10^8	10^2	$\Gamma = 2$
AH2 ...	1	5	10^8	10^2	$\Gamma = 5/3$
B ...	1	1	10^8	10^2	Realistic
BH ...	1	1	10^8	10^2	$\Gamma = 2$
CH ...	1	0.2	10^8	10^2	$\Gamma = 2$
DH ...	0.1	1	10^8	10^2	$\Gamma = 2$
EH ...	0.01	1	10^8	10^2	$\Gamma = 2$
N ...	0	5	10^8	10^2	Realistic
NH ...	0	5	10^8	10^2	$\Gamma = 2$
R ...	1	1	10^6	10^4	Realistic

(a)

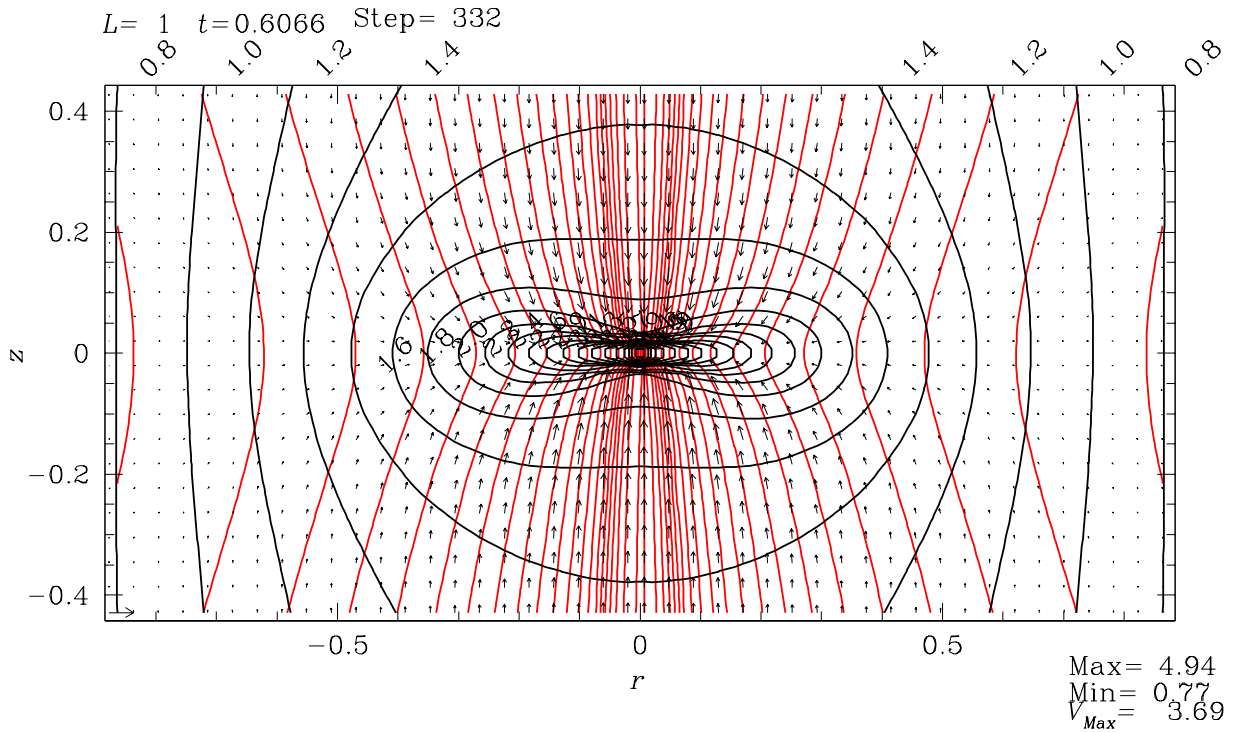
L= 1 t=0.6066 Step= 332
0.8
1.0
1.2
1.4
1.4
1.2
1.0
0.8
0.4
0.2
0
−0.2
−0.4
z
−0.5
0
0.5
r
Max= 4.94
Min= 0.77
V_Max= 3.69

(b)

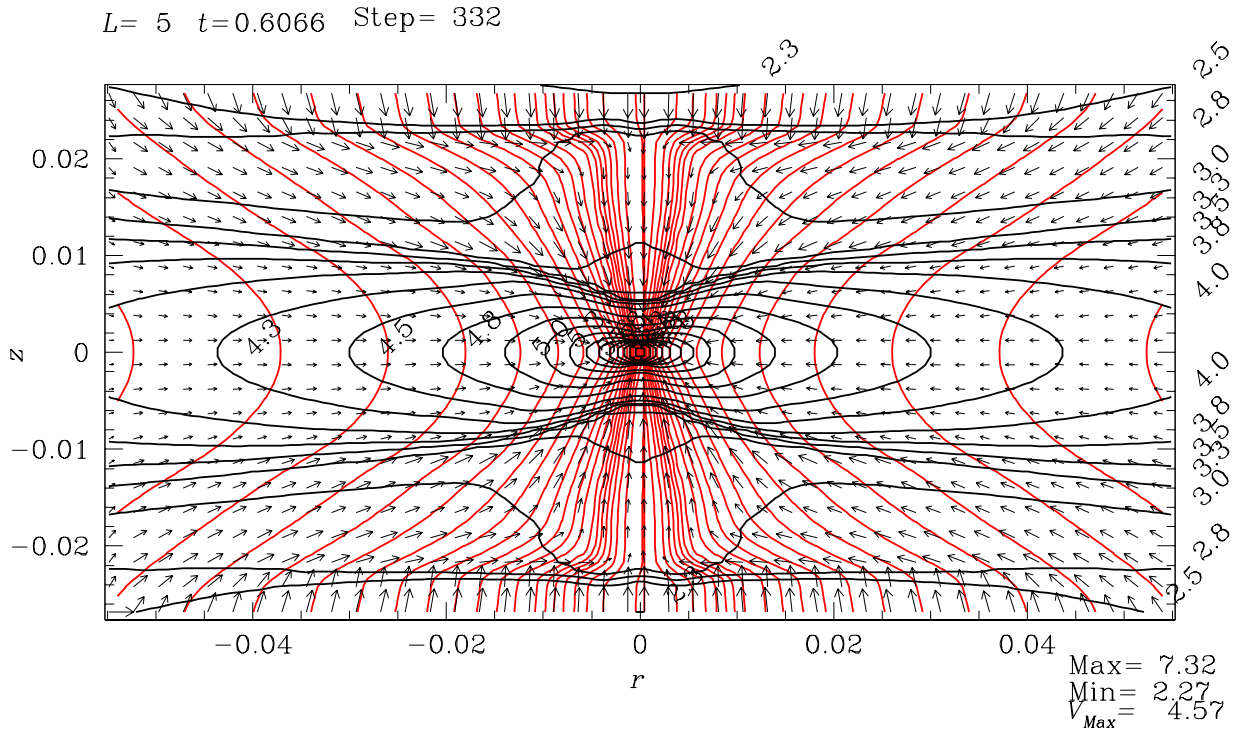
L= 5 t=0.6066 Step= 332
2.3
2.5
2.8
3.0
3.3
3.8
4.0
4.0
3.8
3.3
3.0
2.8
2.5
0.02
0.01
0
−0.01
−0.02
z
4.3
4.5
4.8
−0.04
−0.02
0
0.02
0.04
r
Max= 7.32
Min= 2.27
V_Max= 4.57

(c)

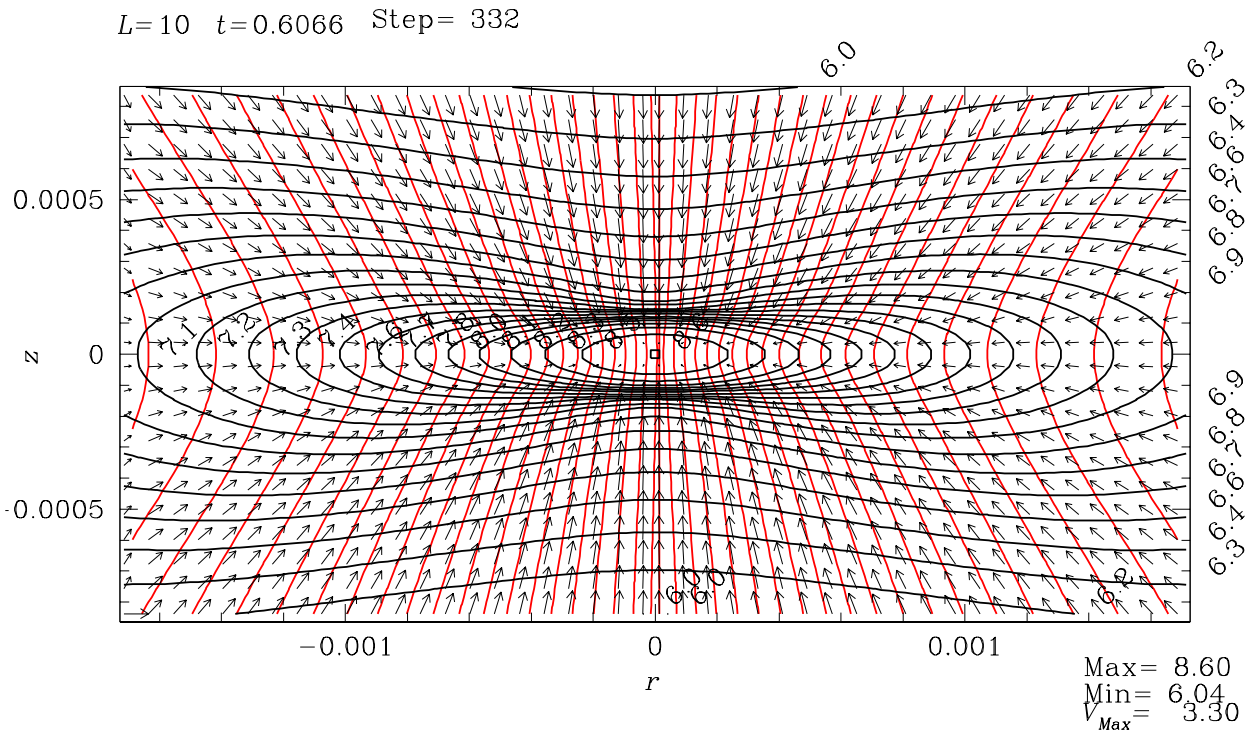

Fig. 1.— Evolution of model A with $\alpha = 1$ and $\Omega_0 = 5$. Snapshots at the time of $t = 0.6066\tau_{\rm ff}$ represented in different levels are shown: L1 (a), L5 (b), and L10 (c). Horizontal and vertical axes represent the r- and z-axis, of which the units are nondimensional. The actual size of the frames of L5 (b) and L10 (c) are, respectively, 1/16 and 1/512 smaller than that of L1 (a). Magnetic field lines (dotted lines) and isodensity contours (solid lines) are presented as well as the velocity vectors by arrows. [In the electronic version, the magnetic field lines are displayed with red solid lines.] Near the right-bottom corner, the logarithm of the maximum and the minimum of the densities are numerically shown. Contour levels are chosen for $\log\rho = \log\rho_{\rm min} + n(\log\rho_{\rm max} - \log\rho_{\rm min})/20$ for nondimensional density ρ with $n = 0, 1, 2, \ldots, 20$. The maximum speed is also shown and the velocity vector corresponding its value is illustrated at the lower-left corner by a horizontal arrow. Level, the elapsed time from the beginning, and the number of time-steps are shown on the top. The time-steps are counted for the coarsest level at that time (L0 for this model). Thus, L1's own time-steps are equal to 332×2^1 and L5's are 332×2^5.

(a)

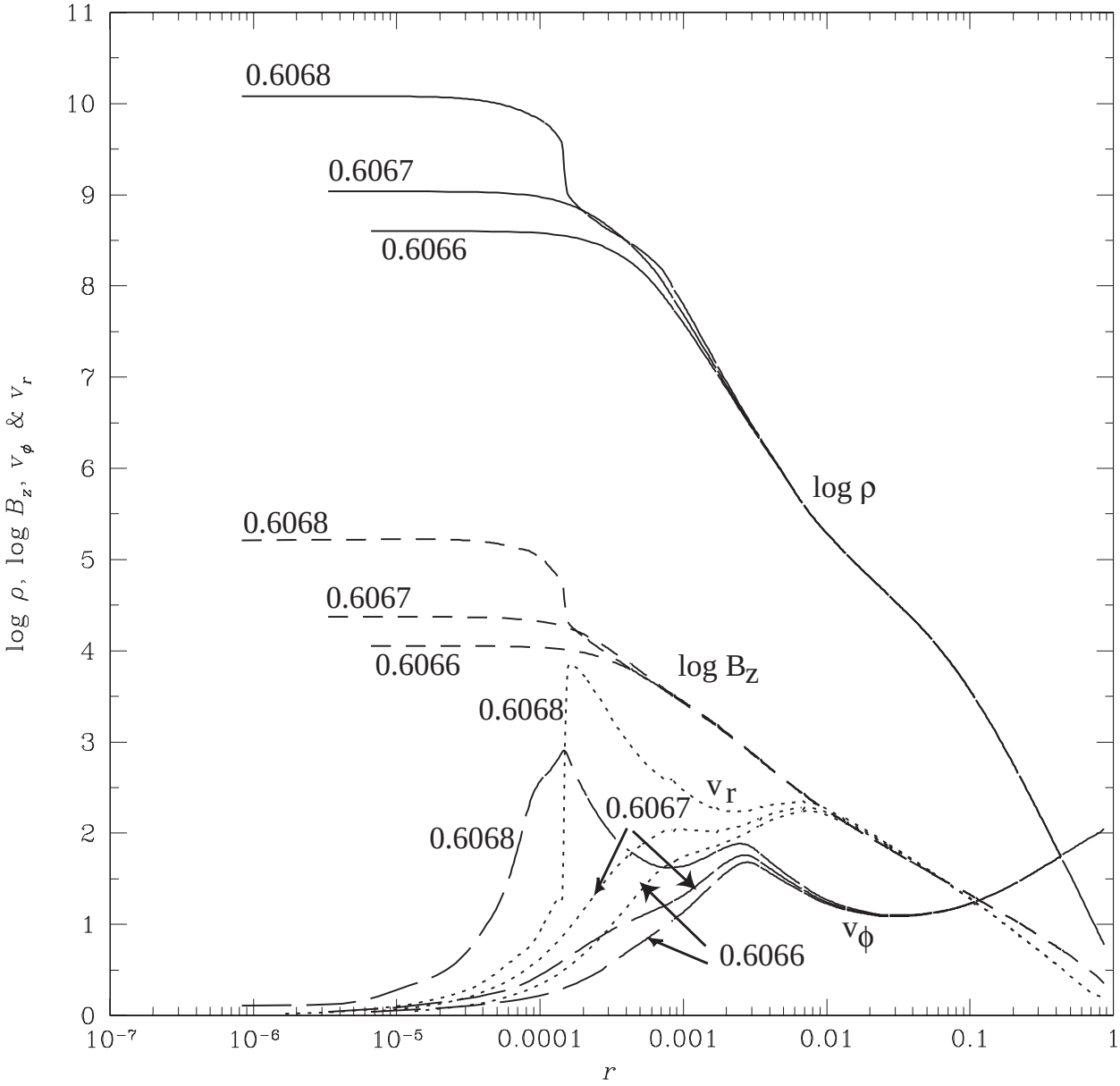
0.6068
0.6067
0.6066
log ρ
0.6068
0.6067
0.6066
log B_z
0.6068
v_r
0.6067
0.6068
v_φ
0.6066
log ρ, log B_z, v_φ & v_r
r
11
10
9
8
7
6
5
4
3
2
1
0
10^-7
10^-6
10^-5
0.0001
0.001
0.01
0.1
1

(b)

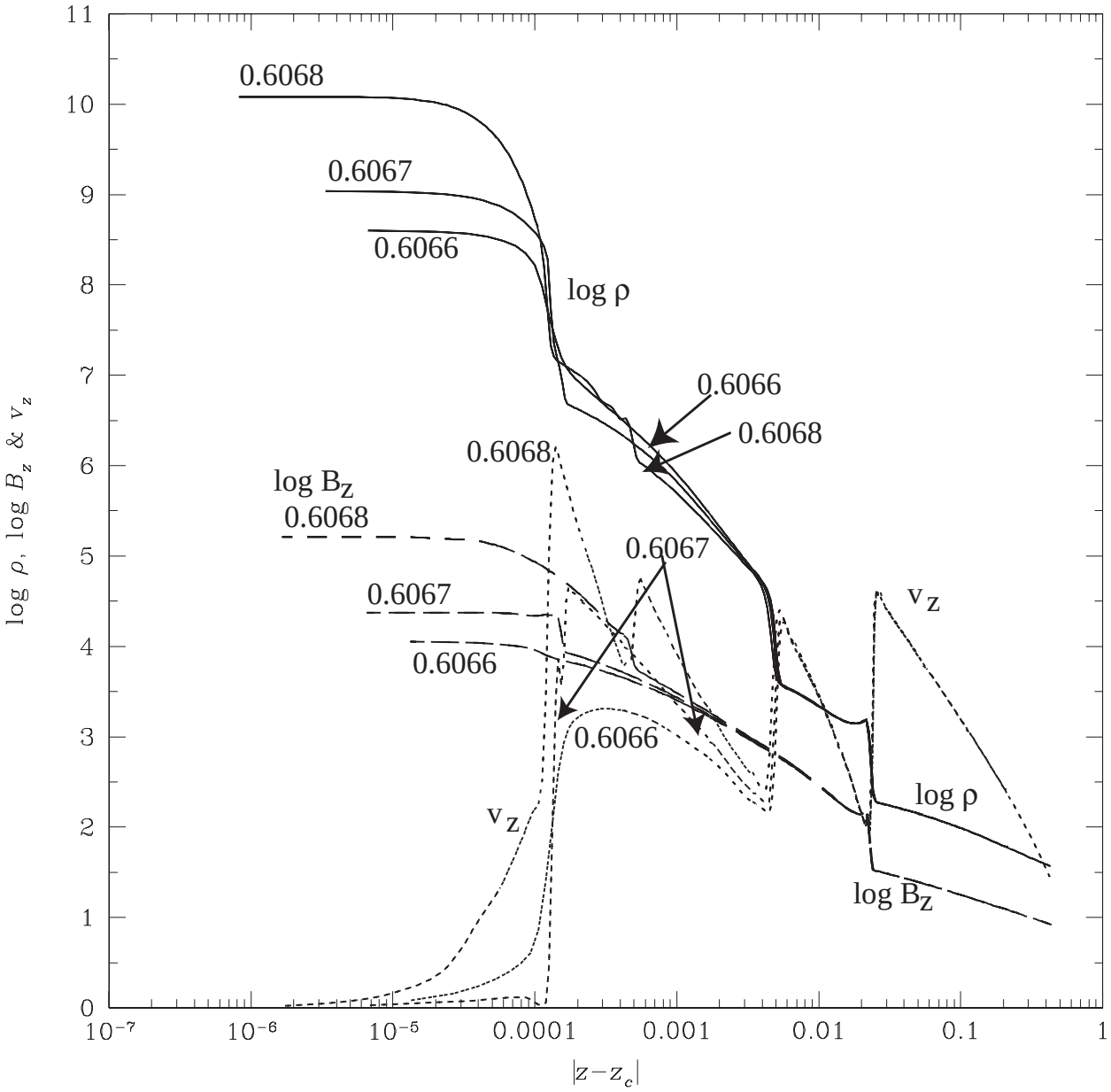

Fig. 2.— Cross-cut views along the equatorial plane (a) and the z-axis (b). All the dependent and independent variables are those of nondimensional units. The figures show the formation of the first core. In panel (a), $\log \rho(r, z = 0)$ (solid lines), $\log B_z(r, z = 0)$ (short dashed lines), $v_\phi(r, z = 0)$ (long dashed lines), and $-v_r(r, z = 0)$ (dotted lines) are plotted, while in panel (b), $\log \rho(r = 0, z)$ (solid lines), $\log B_z(r = 0, z)$ (short dashed lines), and $-v_z(r = 0, z)$ (dotted lines) are plotted.

(a)

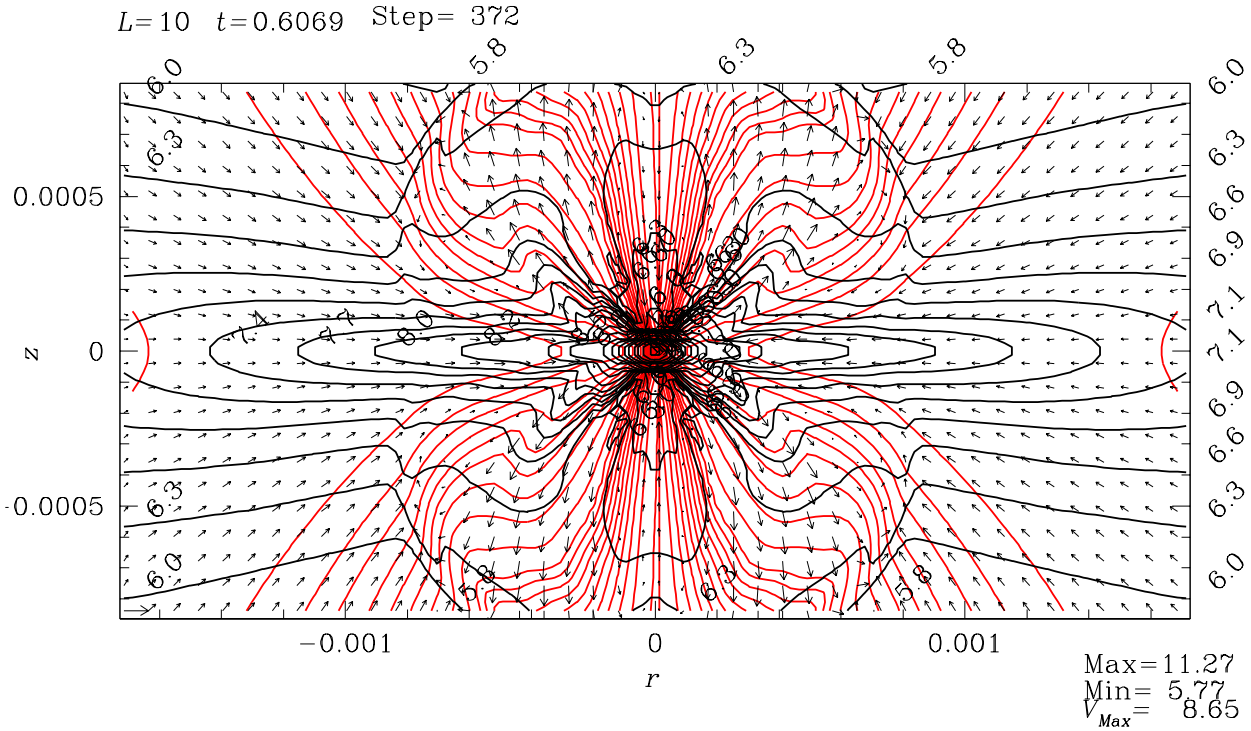
L= 10 t= 0.6069 Step= 372
0.0005
z 0
-0.0005
−0.001
0
0.001
r
Max= 11.27
Min= 5.77
V_Max= 8.65

(b)

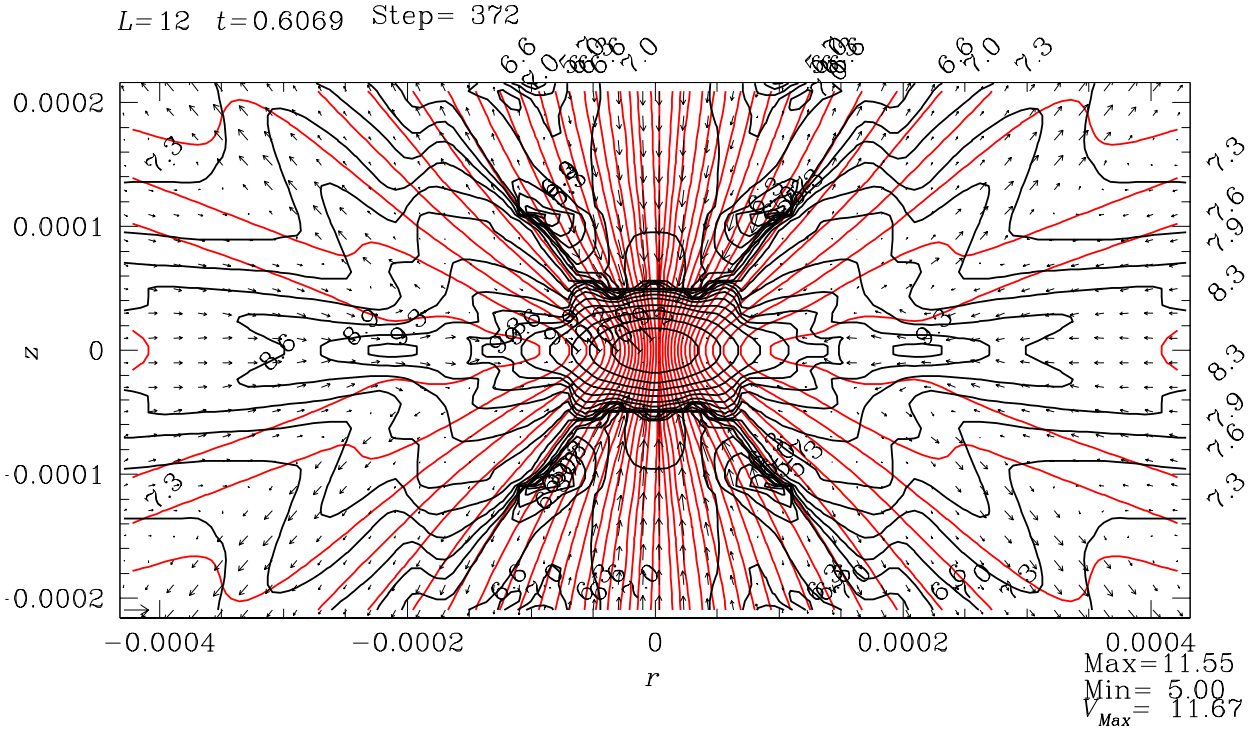
L= 12 t= 0.6069 Step= 372
0.0002
0.0001
z 0
-0.0001
-0.0002
−0.0004
−0.0002
0
0.0002
0.0004
r
Max= 11.55
Min= 5.00
V_Max= 11.67

(c)

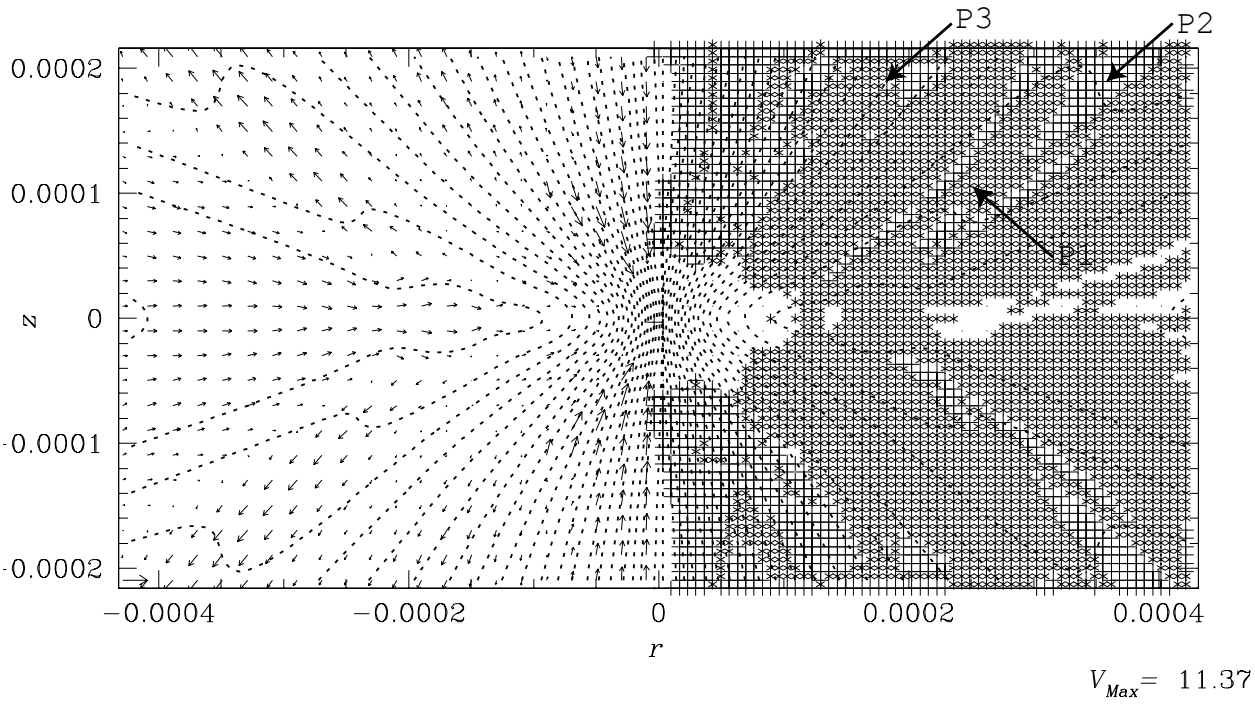

Fig. 3.— The same as Fig.1 but for the snapshot at $t = 0.6069\tau_{\rm ff}$. Panel (a) shows the structure represented in L10 which is the same as Fig.1c. At this stage, gas begins to outflow from the disk. Outflow sweeps the sphere $r \lesssim 1.2 \times 10^{-3} H$. Panel (b) corresponds to L12, which has 4 times finer spatial resolution than panel (a). Panel (c) shows which force is dominant the thermal pressure gradient, the magnetic force (the toroidal magnetic pressure gradient), or the centrifugal force. The components parallel to the magnetic field are compared for each grid point. The symbols "*", "+", and " " (blank) indicate respectively the grid points where the centrifugal force is the largest, the magnetic force is the largest, and the thermal pressure gradient is the largest. In the left, poloidal magnetic field lines and velocity field are shown as panel (b).

(a)

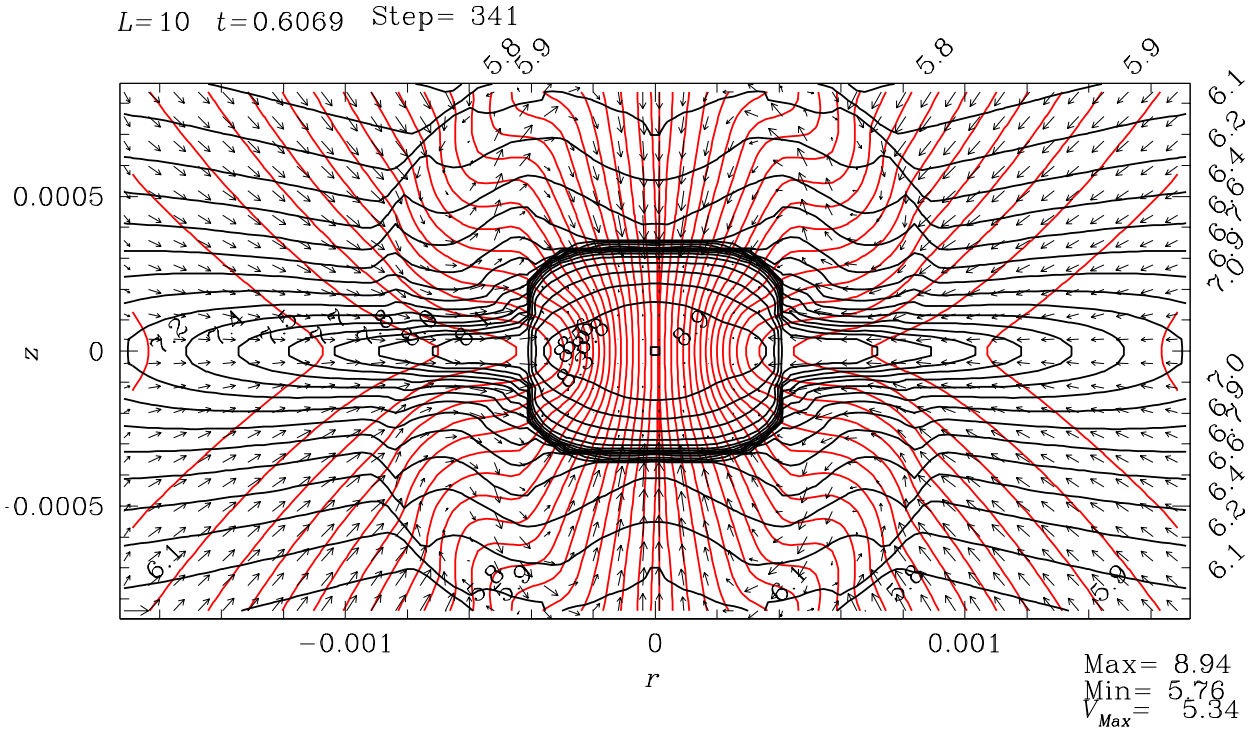
L= 10 t= 0.6069 Step= 341
0.0005
z 0
-0.0005
−0.001
0
0.001
r
Max= 8.94
Min= 5.76
V_Max= 5.34

(b)

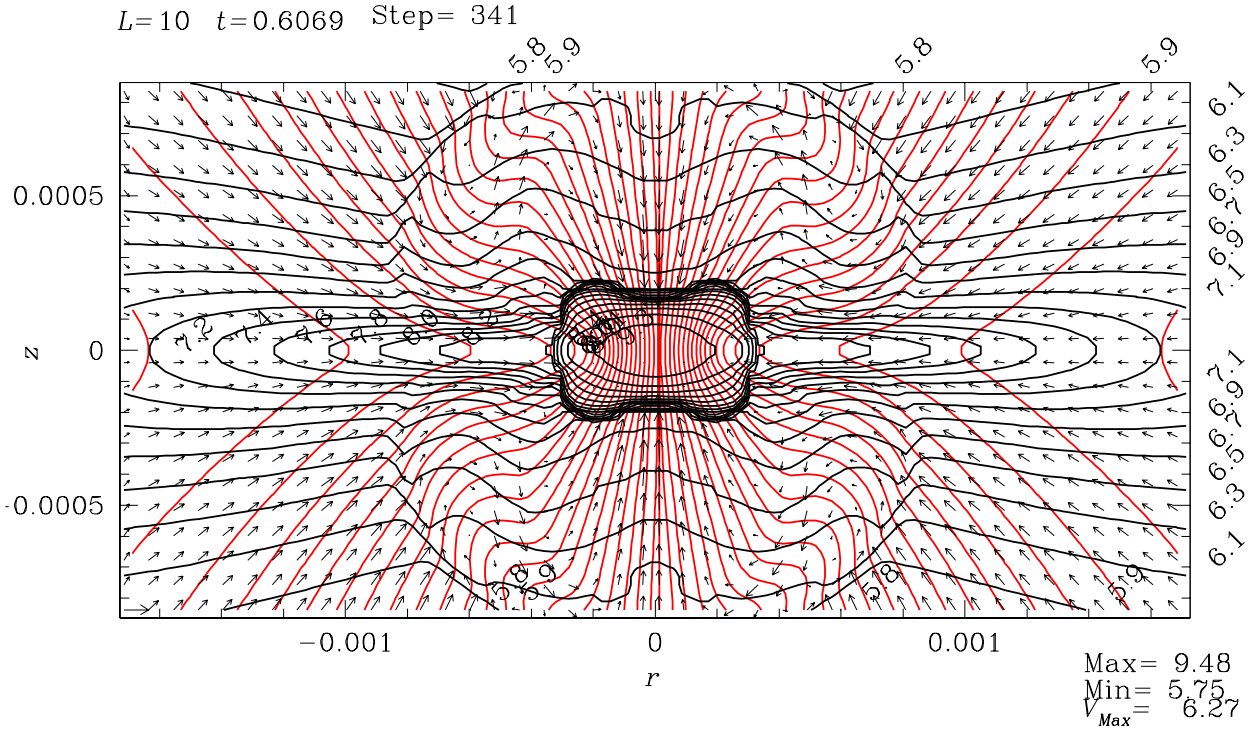
L= 10 t= 0.6069 Step= 341
0.0005
z 0
-0.0005
−0.001
0
0.001
r
Max= 9.48
Min= 5.75
V_Max= 6.27

(c)

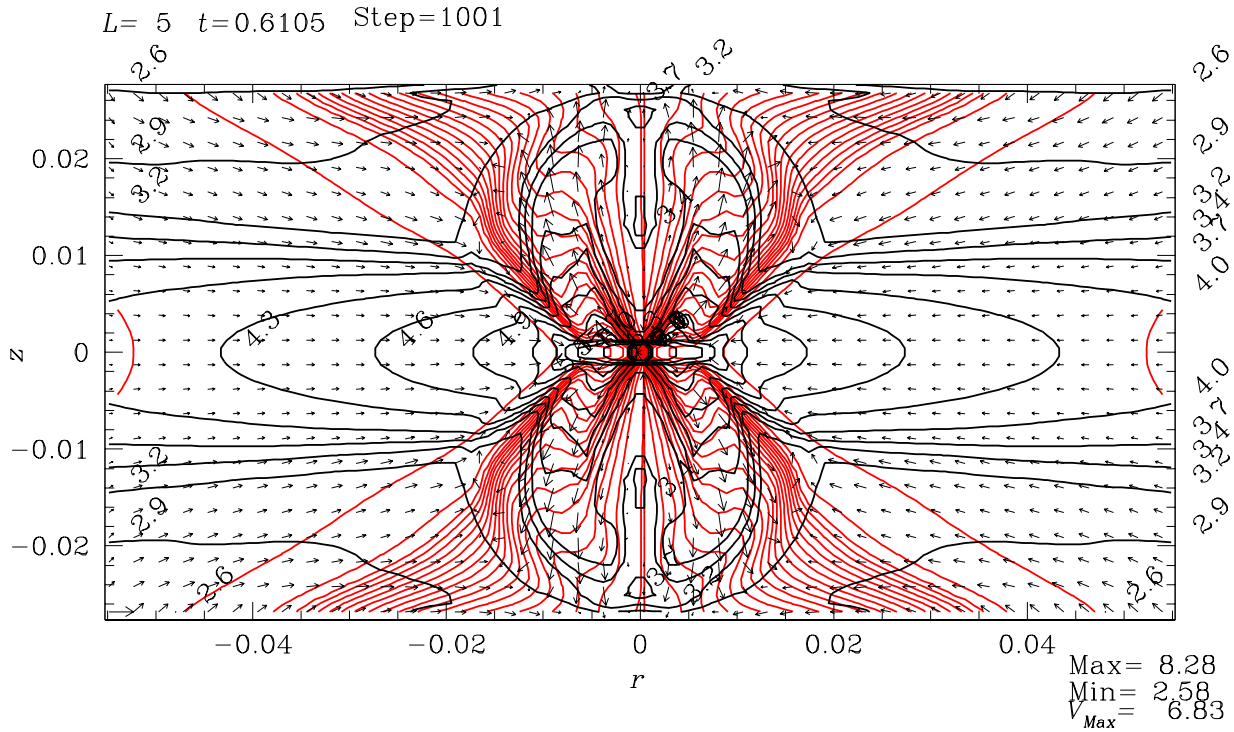

Fig. 4.— The same as Fig.1 but for models AH1 and AH2. Snapshots at the same epoch of Fig.3a, $t = 0.6069\tau_{\rm ff}$, are shown for models AH1 ($\Gamma = 2$) and AH2 ($\Gamma = 5/3$) in panels (a) and (b), respectively. Although the structure of the core is different, the outflow is very similar with each other. In panel (c), snapshot at $t = 0.6105\tau_{\rm ff}$ ($\tau = 3.94 \times 10^{-3}\tau_{\rm ff}$ from the core formation epoch) is plotted for model AH1. Be careful that the linear size of this panel is 32 times larger than panels (a) and (b). Comparing with Fig.1b (the same resolution), it is shown that the shock front passed the slow-mode MHD shock and has just reached the outer fast-mode shock front.

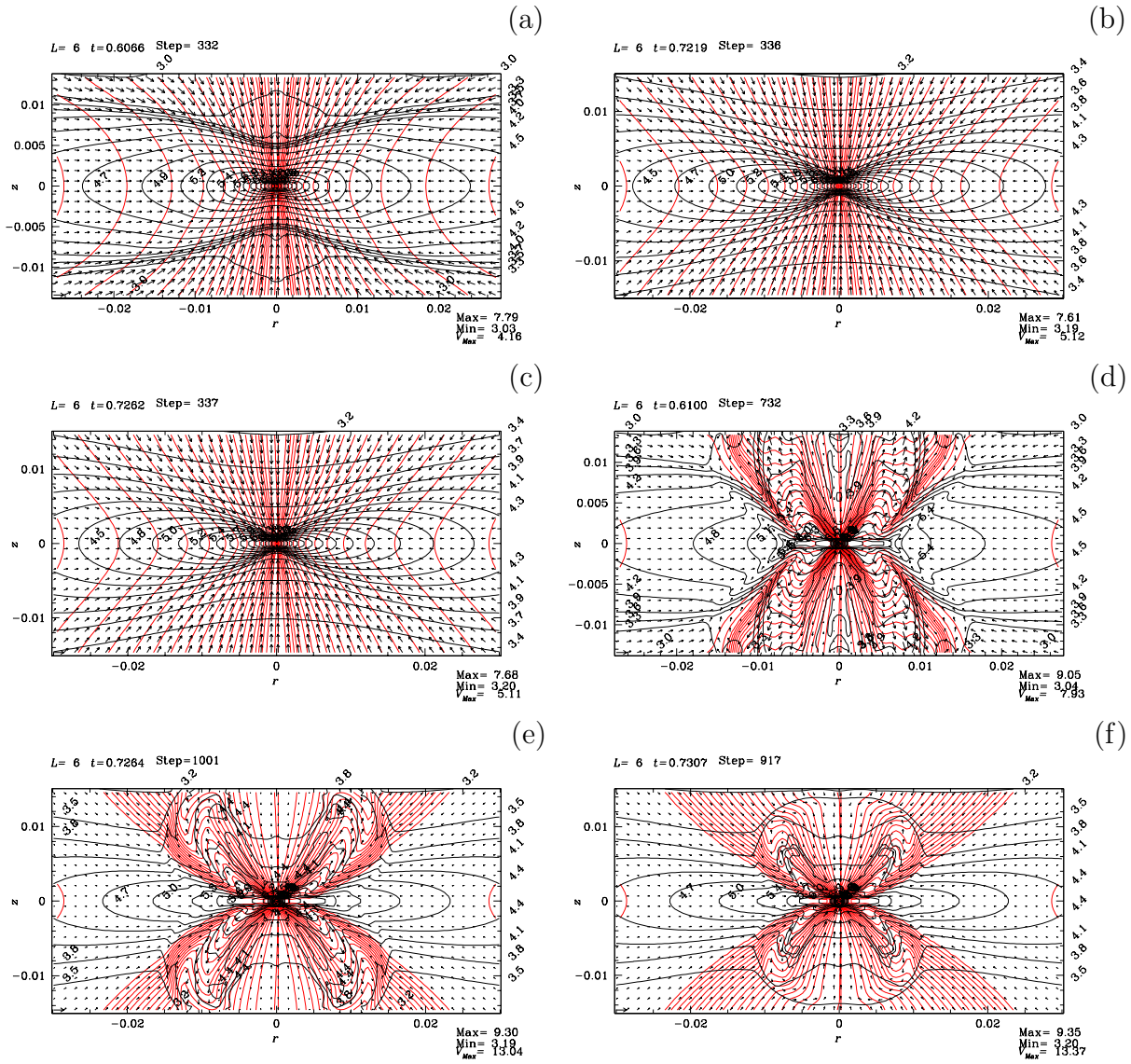

Fig. 5.— Comparison of models with the same magnetic field strength, α, but different rotation speeds, Ω_0. Panels (a) and (d) represent the structure of model AH1 ($\Omega_0 = 5\tau_{\rm ff}^{-1}$) captured by L6. Panels (b) and (e) are for model BH. Model B corresponds to a slower rotator $\Omega_0 = 1\tau_{\rm ff}^{-1}$. Panels (b) and (e) represent the structure captured by L6 at the ages of $t = 0.7219\tau_{\rm ff}$ and $t = 0.7264\tau_{\rm ff}$ ($\tau = 4.5 \times 10^{-3}\tau_{\rm ff}$), respectively. Panels (c) and (f) are for model CH ($\Omega_0 = 0.2\tau_{\rm ff}$) and show the snapshots at $t = 0.7262\tau_{\rm ff}$ and $t = 0.7307\tau_{\rm ff}$ ($\tau = 4.5 \times 10^{-3}\tau_{\rm ff}$), respectively.

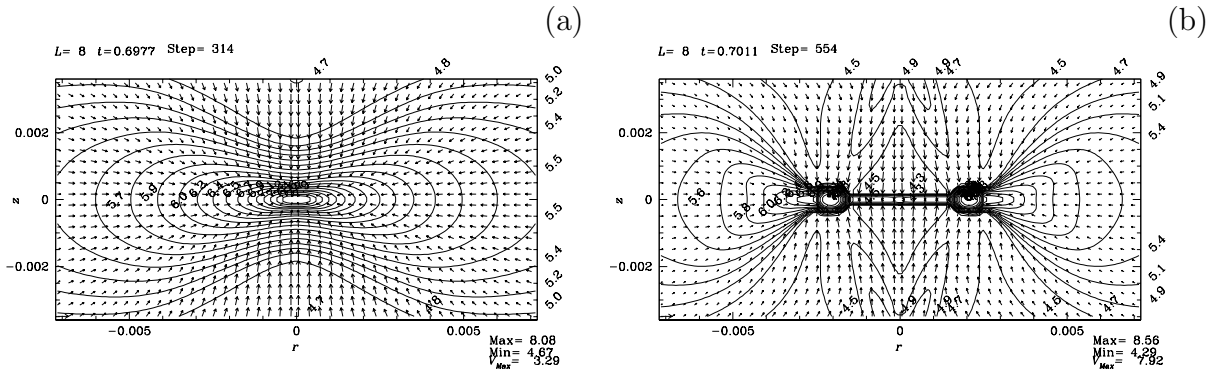

Fig. 6.— The same as Fig.1 but for model NH. This model is for a non-magnetized cloud. In panel (a), a snapshot at $t = 0.6977\tau_{\rm ff}$ represented in L8 is shown. At this stage, whole the cloud is in isothermal regime. Another snapshot at $t = 0.7011\tau_{\rm ff}$ is shown in panel (b). Accreted gas forms a ring which is supported essentially by the centrifugal force.

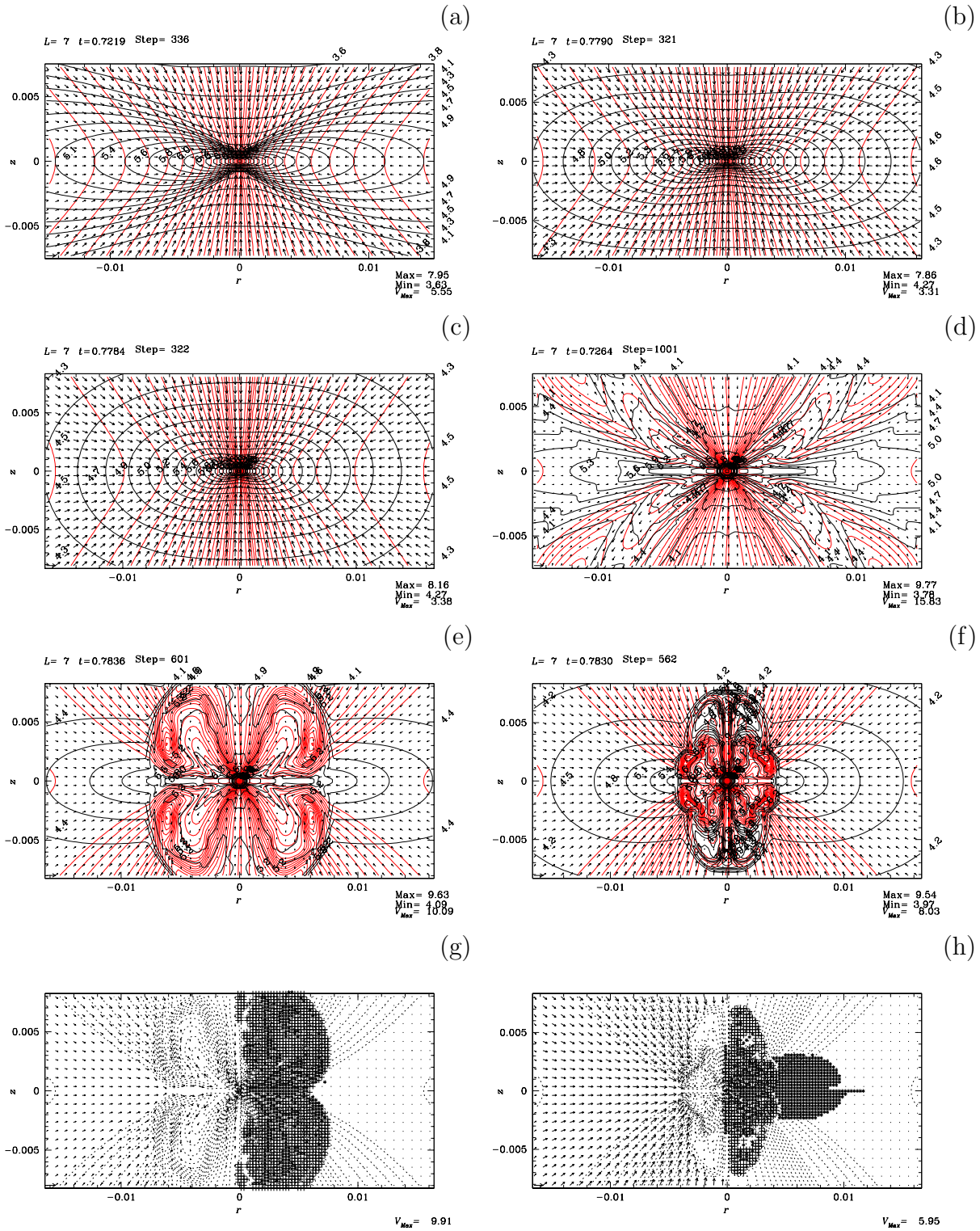

Fig. 7.— Comparison of models with the same rotation speed $\Omega_0 = 1$ but different magnetic

field strengths α. Panels (a), (b), and (c) represent the structure when the adiabatic core begins to form, while panels (d), (e), and (f) represent the structure after a protostar is formed. In panel (a), we plotted a snapshot for model BH captured by L7 at $t = 0.7219\tau_{\rm ff}$, which is the same snapshot shown in Fig.5b but for different level. Panel (d) represents the structure of the same model but for the protostellar phase, that is, $t = 0.7264\tau_{\rm ff}$ ($\tau = 4.46 \times 10^{-3}\tau_{\rm ff}$). This corresponds to Figure 5e. Panels (b) and (e) illustrate snapshots at $t = 0.7790\tau_{\rm ff}$ and at $t = 0.7836\tau_{\rm ff}$ ($\tau = 4.59 \times 10^{-3}\tau_{\rm ff}$), respectively, for model DH ($\alpha = 0.1$). Panels (c) and (f) are for a model with extremely weak magnetic fields (model EH; $\alpha = 0.01$). The snapshots at the epoch $t = 0.7784\tau_{\rm ff}$ and $t = 0.7830\tau_{\rm ff}$ ($\tau = 4.53\times10^{-3}\tau_{\rm ff}$) are illustrated in panels (c) and (f), respectively. Panels (g) and (h) are the same figure as Fig.3(c) but for models DH and EH. Panel (g) shows the distribution at the same epoch of panel (e). This indicates that near the disk the centrifugal force is dominated (region C) $|z| \lesssim 5 \times 10^{-3}H$. Above $|z| \gtrsim 5 \times 10^{-3}H$, region M is mainly distributed. Compared with Fig.3c of model A, the magnetic force plays more important role for models with low α. Panel (h), which shows the force distributions at the same epoch of panel (f), indicates that magnetic force-dominated region is predominantly distributed in the magnetic bubble for $|z| \gtrsim 3 \times 10^{-3}H$. This means that the magnetic force plays a major role in the magnetic bubble for model EH.

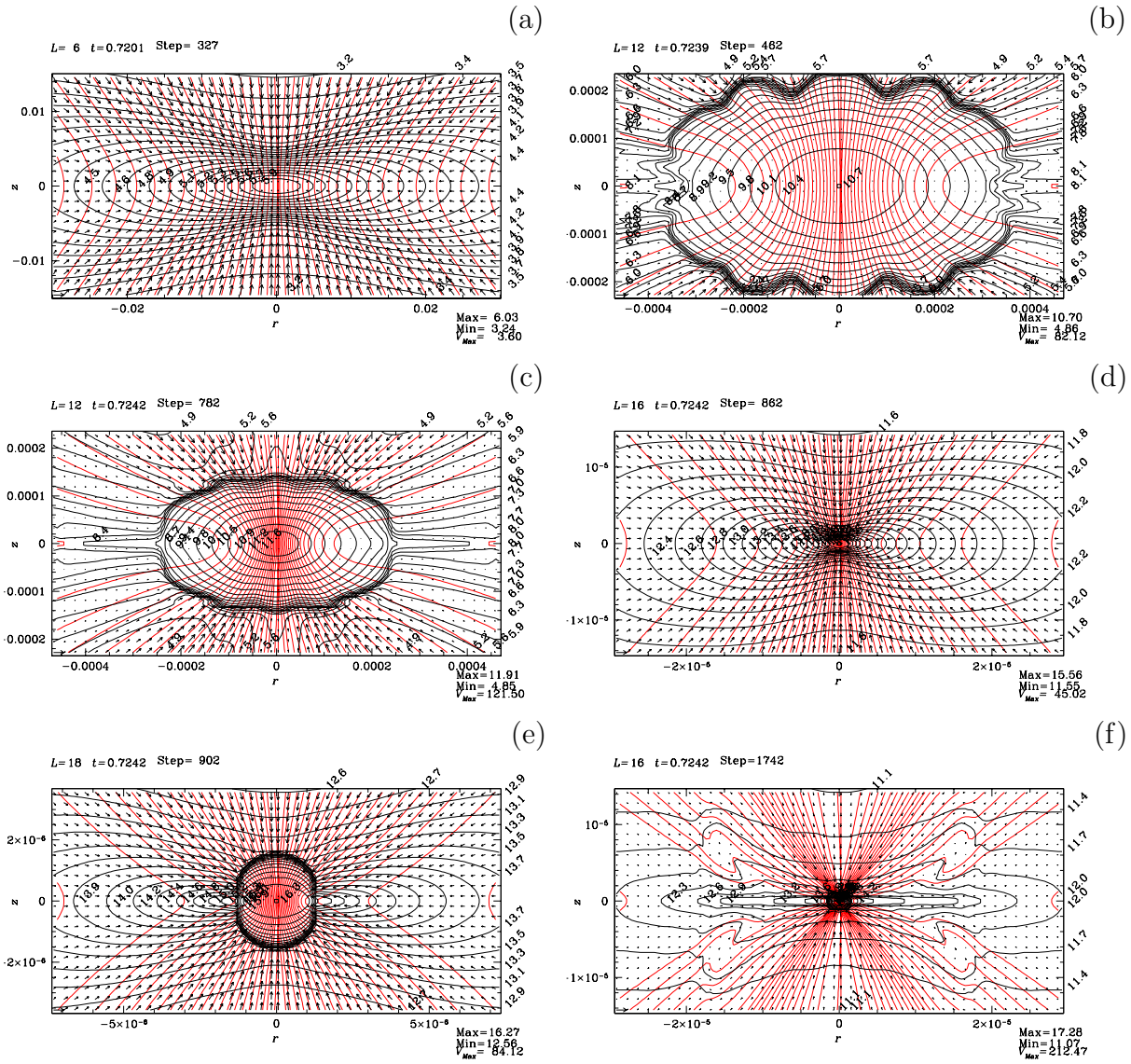

Fig. 8.— The evolution of model R. In this model since ρ_s is assumed equal to $10^4 \mathrm{H_2\,cm^{-3}}$, the size scale H is 10-times smaller than other models with $\rho_s = 10^2 \mathrm{H_2\,cm^{-3}}$. In panel (a), we plotted the structure represented in L6 just before the first core formation $t = 0.7201\tau_{\rm ff}$. At $t = 0.7239\tau_{\rm ff}$ ($\tau = 3.8 \times 10^{-3}\tau_{\rm ff}$), the first core gradually contracts by the effect of continuous mass accretion (panel b). Finally, $t = 0.724230\tau_{\rm ff}$ ($\tau = 4.132 \times 10^{-3}\tau_{\rm ff}$), the central density reaches $\rho_{\rm B}$ (panel c). After that, the second collapse begins. In this phase, flow is very similar to that realized in the isothermal run-away collapse phase. In panel (d), we plotted the structure captured in L16 at $t = 0.724236\tau_{\rm ff}$ ($\tau = 4.138 \times 10^{-3}\tau_{\rm ff}$). After the central density exceeds $\rho_{\rm C}$, another adiabatic core (the second core) is formed (panel e). By a similar mechanism to form a bipolar outflow, a second outflow is formed around the second core

(panel f). This is a snapshot of L16 at $t = 0.724237\tau_{\rm ff}$ ($\tau = 4.140 \times 10^{-3}\tau_{\rm ff}$).

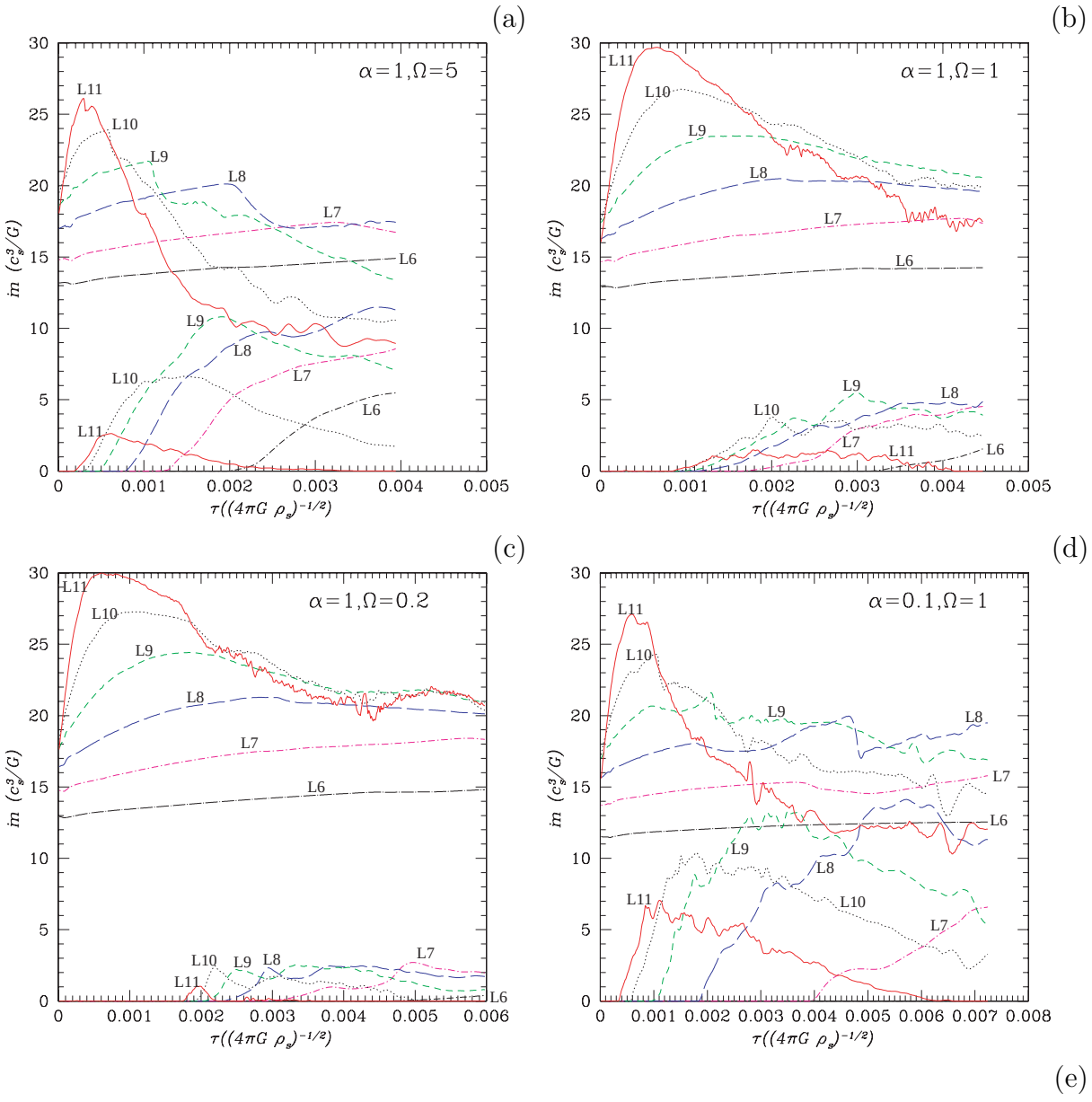
(a)
α=1,Ω=5
L11
L10
L9
L8
L7
L6
ṁ (c_s^3/G)
τ((4πG ρ_s)^-1/2)
(b)
α=1,Ω=1
(c)
α=1,Ω=0.2
(d)
α=0.1,Ω=1
(e)

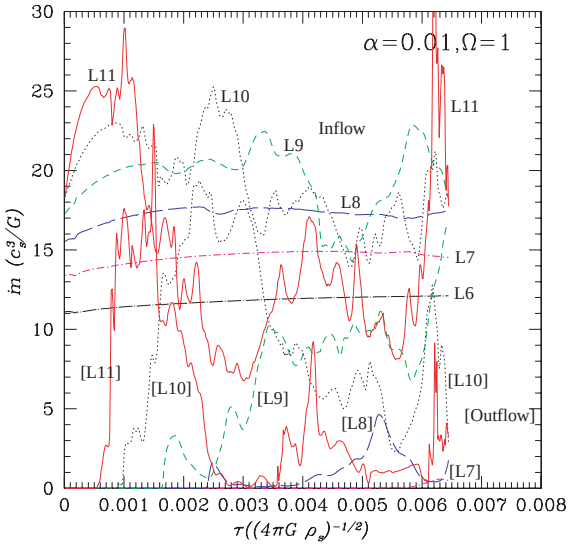

Fig. 9.— Mass inflow/outflow rates calculated at the boundaries of nested grid systems (eqs.32 and 31). Panel (a)-(e) corresponds to models AH1, BH, CH, DH, and EH. The horizontal axis represents the time after the core formation. Levels at which the mass inflow/outflow rates are calculated are shown near the respective lines. We plotted L11 in a solid line, L10 in a dotted line, L9 in a short-dashed line, L8 in a long-dashed line, L7 in a short dash-dotted line, and L6 in a long dash-dotted line. In panel (e) to specify which line represents the outflow, we added brackets to the outflow rates. Inflow rates are larger than outflow rates for respective levels.

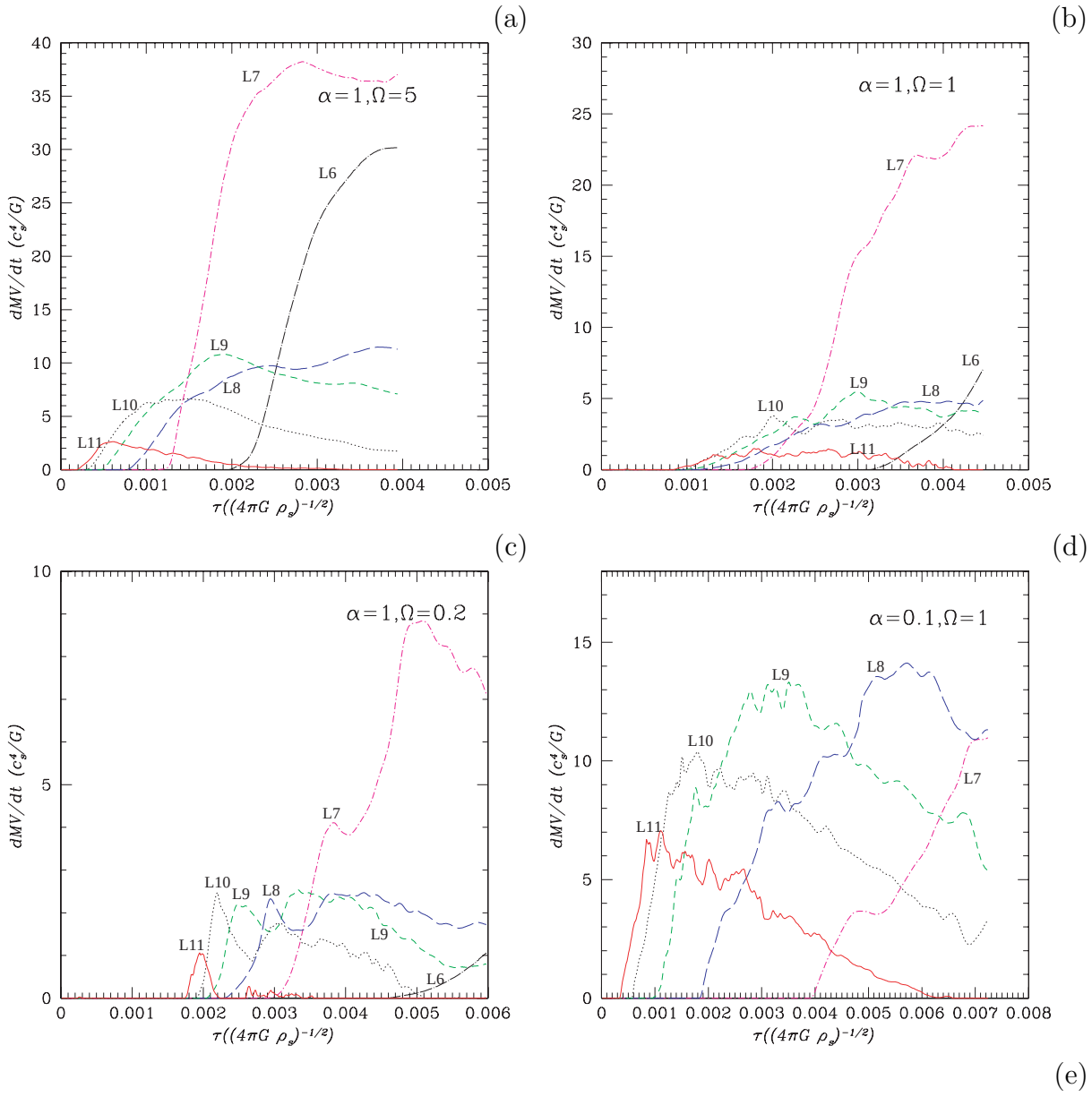
(a)
α=1,Ω=5
L7
L6
L9
L8
L10
L11
dMV/dt (c_s^4/G)
τ((4πG ρ_s)^-1/2)
(b)
α=1,Ω=1
L7
L6
L9
L8
L10
L11
dMV/dt (c_s^4/G)
τ((4πG ρ_s)^-1/2)
(c)
α=1,Ω=0.2
L7
L10
L9
L8
L11
L9
L6
dMV/dt (c_s^4/G)
τ((4πG ρ_s)^-1/2)
(d)
α=0.1,Ω=1
L9
L8
L10
L7
L11
dMV/dt (c_s^4/G)
τ((4πG ρ_s)^-1/2)
(e)

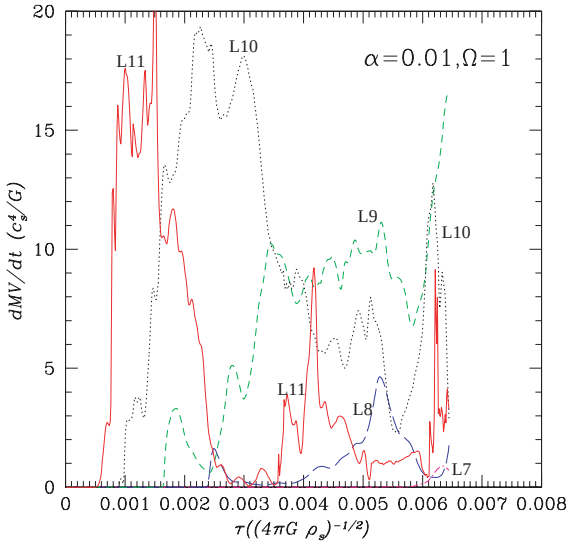

Fig. 10.— Linear momentum outflow rates calculated at the upper and lower boundaries of nested grid systems (eqs.33). Panel (a)-(e) corresponds to models AH1, BH, CH, DH, and EH. The horizontal axis represents the time after the core formation. Levels at which the linear momentum outflow rates are measured are shown near the respective lines. We plotted L11 in a solid line, L10 in a dotted line, L9 in a short-dashed line, L8 in a long-dashed line, L7 in a short dash-dotted line, and L6 in a long dash-dotted line.